How accurately can 21 cm tomography constrain cosmology?

Yi Mao,[1,*] Max Tegmark,[1,2,+] Matthew McQuinn,[3] Matias Zaldarriaga,[3,4] and Oliver Zahn[3,5]

[1]*Center for Theoretical Physics, Department of Physics, Massachusetts Institute of Technology, Cambridge, Massachusetts 02139, USA*

[2]*MIT Kavli Institute for Astrophysics and Space Research, Cambridge, Massachusetts 02139, USA*

[3]*Harvard-Smithsonian Center for Astrophysics, 60 Garden Street, Cambridge, Massachusetts 02138, USA*

[4]*Jefferson Laboratory of Physics, Harvard University, Cambridge, Massachusetts 02138, USA*

[5]*Berkeley Center for Cosmological Physics, Department of Physics, University of California, and Lawrence Berkeley National Labs, 1 Cyclotron Road, Berkeley, California 94720, USA*

(Received 21 February 2008; published 25 July 2008)

There is growing interest in using 3-dimensional neutral hydrogen mapping with the redshifted 21 cm line as a cosmological probe. However, its utility depends on many assumptions. To aid experimental planning and design, we quantify how the precision with which cosmological parameters can be measured depends on a broad range of assumptions, focusing on the 21 cm signal from $6 < z < 20$. We cover assumptions related to modeling of the ionization power spectrum, to the experimental specifications like array layout and detector noise, to uncertainties in the reionization history, and to the level of contamination from astrophysical foregrounds. We derive simple analytic estimates for how various assumptions affect an experiment's sensitivity, and we find that the modeling of reionization is the most important, followed by the array layout. We present an accurate yet robust method for measuring cosmological parameters that exploits the fact that the ionization power spectra are rather smooth functions that can be accurately fit by 7 phenomenological parameters. We find that for future experiments, marginalizing over these nuisance parameters may provide constraints almost as tight on the cosmology as if 21 cm tomography measured the matter power spectrum directly. A future square kilometer array optimized for 21 cm tomography could improve the sensitivity to spatial curvature and neutrino masses by up to 2 orders of magnitude, to $\Delta\Omega_k \approx 0.0002$ and $\Delta m_\nu \approx 0.007$ eV, and give a 4σ detection of the spectral index running predicted by the simplest inflation models.

DOI: 10.1103/PhysRevD.78.023529 PACS numbers: 98.80.Es, 98.58.Ge

I. INTRODUCTION

Three-dimensional mapping of our Universe using the redshifted 21 cm hydrogen line has recently emerged as a promising cosmological probe, with arguably greater long-term potential than the cosmic microwave background (CMB). The information garnered about cosmological parameters grows with the volume mapped, so the ultimate goal for the cosmology community is to map our entire horizon volume, the region from which light has had time to reach us during the 14×10^9 years since our big bang. Figure 1 illustrates that, whereas the CMB mainly probes a thin shell from $z \sim 1000$, and current large-scale structure probes (like galaxy clustering, gravitational lensing, type Ia supernovae, and the Lyman α forest) only map small volume fractions nearby, neutral hydrogen tomography is able to map most of our horizon volume.

Several recent studies have forecast the precision with which such 21 cm tomography can constrain cosmological parameters, both by mapping diffuse hydrogen before and during the reionization epoch [1–3] and by mapping neutral hydrogen in galactic halos after reionization [4]. These studies find that constraints based on the cosmic microwave background measurements can be significantly improved. However, all of these papers make various assumptions, and it is important to quantify to what extent their forecasts depend on these assumptions. This issue is timely because 21 cm experiments (like LOFAR [5], 21CMA [6], MWA [7], and SKA [8]) are still largely in their planning, design, or construction phases. These experiments will be described in detail in Sec. II G. In order to maximize their scientific "bang for the buck," it is therefore important to quantify how various design tradeoffs affect their sensitivity to cosmological parameters.

The reason that neutral hydrogen allows mapping in three rather than two dimensions is that the redshift of the 21 cm line provides the radial coordinate along the line-of-sight (l.o.s.). This signal can be observed from the so-called dark ages [9,10] before any stars had formed, through the epoch of reionization (EoR), and even to the current epoch (where most of the neutral hydrogen is confined within galaxies). We focus in this study on the 21 cm signal from $6 < z < 20$—the end of the dark ages through the EoR. This is the redshift range at which the synchrotron foregrounds are smallest, and consequently it is the range most assessable for all planned 21 cm arrays.

There are three position-dependent quantities that imprint signatures on the 21 cm signal: the hydrogen density, the neutral fraction, and the spin temperature. For cosmo-

*ymao@mit.edu
+tegmark@mit.edu

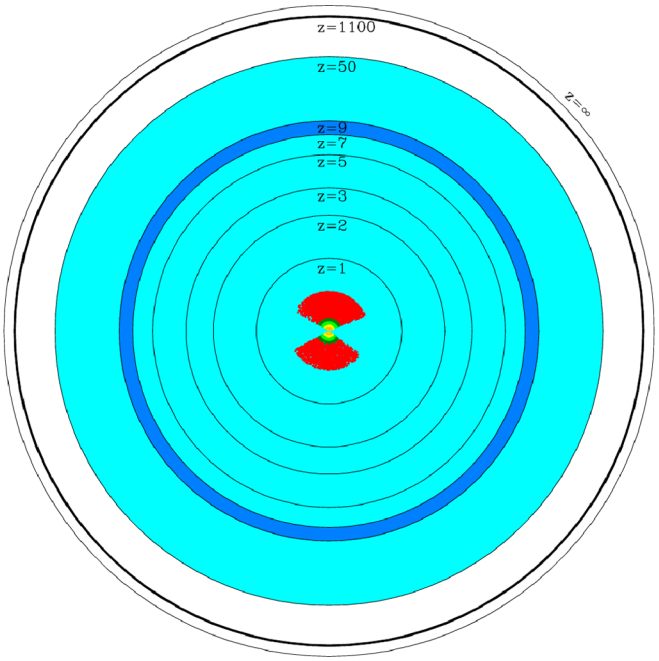

FIG. 1 (color online). The 21 cm tomography can potentially map most of our observable Universe (light blue/light gray), whereas the CMB probes mainly a thin shell at $z \sim 10^3$ and current large-scale structure surveys (here exemplified by the Sloan Digital Sky Survey and its luminous red galaxies) map only small volumes near the center. This paper focuses on the convenient $7 \lesssim z \lesssim 9$ region (dark blue/dark gray).

TABLE I. Factors that affect the cosmological parameter measurement accuracy.

Assumptions		Pessimistic	Middle	Optimistic
Power modeling	Ionization power spectrum modeling	Marginalize over arbitrary P_{μ^0} and P_{μ^2}	Marginalize over constants that parametrize $\mathcal{P}_{xx}(k)$ and $\mathcal{P}_{x\delta}(k)$	No ionization power spectrum, $\mathcal{P}_{\delta\delta}(k) \propto P_{\Delta T}(\mathbf{k})$.
	Nonlinear cutoff scale $k_{\max}$	1 Mpc^{-1}	2 Mpc^{-1}	4 Mpc^{-1}
	Non-Gaussianity of ionization signals	Doubles sample variance	Negligible	
Cosmological	Reionization history	Gradual reionization over a wide range of redshifts		Abrupt reionization at $z \lesssim 7$
	Redshift range	7.3–8.2	6.8–8.2	6.8–10
	Parameter space	Vanilla model plus optional parameters		Vanilla model parameters
Experimental	Data	MWA, LOFAR, 21CMA	Intermediate case	SKA, FFTT
	Array configuration[a]	$\eta = 0.15$	$\eta = 0.8$, $n = 2$	Giant core
	Collecting area[b]	$0.5 \times$ design values	Design values	$2 \times$ design values
	Observation time[c]	1000 hours	4000 hours	16 000 hours
	System temperature	$2 \times T_{\rm sys}$ in [17]	$T_{\rm sys}$ given in [17]	$0.5 \times T_{\rm sys}$ in [17]
Astrophysical	Residual foregrounds cutoff scale $k_{\min}$[d]	$4\pi/yB$	$2\pi/yB$	π/yB

[a]For the FFTT, we consider only the case where all dipoles are in a giant core.
[b]See designed or assumed values of A_e in Table IV.
[c]Assumes observation of two places in the sky.
[d]It is hard to predict the level of the residual foregrounds after the removal procedure. To quantify contributions from other factors, we take the approximation that there is no residual foregrounds at $k > k_{\min}$. Here in the table, yB is the comoving (l.o.s.) distance width of a single z bin.

logical parameter measurements, only the first quantity is of interest, and the last two are nuisances. (For some astronomical questions, the situation is reversed.) The 21 cm spin-flip transition of neutral hydrogen can be observed in the form of either an absorption line or an emission line against the CMB blackbody spectrum, depending on whether the spin temperature is lower or higher than the CMB temperature.

During the epoch of reionization, the spin temperature is likely coupled to the gas temperature through Lyα photons via the Wouthuysen-Field effect [11,12], and the gas in the intergalactic medium (IGM) has been heated by x-ray photons to hundreds of Kelvin from the first stars [13]. If this is true, the 21 cm signal will only depend on the hydrogen density and the neutral fraction. However, astrophysical uncertainties prevent a precise prediction for exactly when the gas is heated to well above the CMB temperature and is coupled to the spin temperature. In this paper, we follow [1,2] and focus entirely on the regime when the spin temperature is much larger than the CMB temperature [14–16], such that the observed signal depends only on fluctuations in density and/or the neutral fraction. Specifically, we focus on the time interval from when this approximation becomes valid (around the beginning of the reionization [14–16]) until most hydrogen has become ionized, illustrated by the darkest region in Fig. 1. Despite this simplification, the methods that we apply to model the ionization fluctuations almost certainly can be applied to model spin temperature fluctuations with minimal additional free parameters.

In Table I, we list all the assumptions that affect the accuracy of cosmological parameter measurements, including ones about power modeling, cosmology, experimental design, and astrophysical foregrounds. For each case, we provide three categories of assumptions: pessimistic (PESS), middle-of-the-road (MID), and optimistic (OPT). Since we wish to span the entire range of uncertainties, we have made both the PESS and OPT models rather extreme. The MID model is intended to be fairly realistic, but somewhat on the conservative (pessimistic) side.

Before describing these assumptions in detail in the next section, it is important to note that, taken together, they make a huge difference. Table II illustrates this by showing the cosmological parameter constraints resulting from using all the OPT assumptions, all the MID assumptions, or all the PESS assumptions, respectively. For example, combining CMB data from Planck and 21 cm data from the Fast Fourier Transform Telescope (FFTT), the 1σ uncertainty differs by a factor of 125 for Ω_k and by a factor of 61 for m_ν depending on assumptions. It is therefore important to sort out which of the assumptions contribute the most to these big discrepancies, and which assumptions do not matter much. This is a key goal of our paper.

The rest of this paper is organized as follows. In Sec. II, we explain in detail the assumptions in the same order as in Table I, and also present a new method for modeling the ionization power spectra. In Sec. III, we quantify how the cosmological parameter measurement accuracy depends on each assumption, and we derive simple analytic approx-

TABLE II. The dependence of cosmological constraints on the full range of assumptions. We assume the fiducial values given in Sec. II F, and employ the Fisher matrix formalism to forecast the 1σ accuracy of 21 cm tomography measurements. Unless otherwise noted, errors are computed by marginalizing over all other parameters in the first ten columns (which we refer to as the vanilla parameters). In "All OPT/MID/PESS," we use the assumptions of the right, middle, and left columns of Table I, respectively. We assume that the total observing time is split between two sky regions, each for an amount in Table I, using a giant/quasigiant/small core array configuration where 100%/80%/15% of the antennae in the inner core are compactly laid at the array center, while the rest, 0%/20%/85%, of antennae fall off in density as $\rho \sim r^{-2}$ outside the compact core.

		Vanilla alone												
		$\Delta\Omega_\Lambda$	$\Delta \ln(\Omega_m h^2)$	$\Delta \ln(\Omega_b h^2)$	Δn_s	$\Delta \ln A_s$	$\Delta\tau$	$\Delta\bar{x}_H(7.0)$[a]	$\Delta\bar{x}_H(7.5)$	$\Delta\bar{x}_H(8.0)$	$\Delta\bar{x}_H(9.2)$	$\Delta\Omega_k$	Δm_ν (eV)	$\Delta\alpha$
Planck		0.0070	0.0081	0.0059	0.0033	0.0088	0.0043	...	...	...	...	0.025	0.23	0.0026
+LOFAR	All OPT	0.0044	0.0052	0.0051	0.0018	0.0087	0.0042	0.0063	0.0063	0.0063	0.0063	0.0022	0.023	0.000 73
	All MID	0.0070	0.0081	0.0059	0.0032	0.0088	0.0043	0.18	0.26	0.23	...	0.018	0.22	0.0026
	All PESS	0.0070	0.0081	0.0059	0.0033	0.0088	0.0043	...	51	49	...	0.025	0.23	0.0026
+MWA	All OPT	0.0063	0.0074	0.0055	0.0024	0.0087	0.0043	0.0062	0.0062	0.0062	0.0062	0.0056	0.017	0.000 54
	All MID	0.0061	0.0070	0.0056	0.0030	0.0087	0.0043	0.32	0.22	0.29	...	0.021	0.19	0.0026
	All PESS	0.0070	0.0081	0.0059	0.0033	0.0088	0.0043	...	29	30	...	0.025	0.23	0.0026
+SKA	All OPT	0.000 52	0.0018	0.0040	0.000 39	0.0087	0.0042	0.0059	0.0059	0.0059	0.0059	0.0011	0.010	0.000 27
	All MID	0.0036	0.0040	0.0044	0.0025	0.0087	0.0043	0.0094	0.014	0.011	...	0.0039	0.056	0.0022
	All PESS	0.0070	0.0081	0.0059	0.0033	0.0088	0.0043	...	1.1	1.0	...	0.025	0.23	0.0026
+FFTT[b]	All OPT	0.000 10	0.0010	0.0029	0.000 088	0.0086	0.0042	0.0051	0.0051	0.0051	0.0051	0.000 20	0.0018	0.000 054
	All MID	0.000 38	0.000 34	0.000 59	0.000 33	0.0086	0.0042	0.0013	0.0022	0.0031	...	0.000 23	0.0066	0.000 17
	All PESS	0.0070	0.0081	0.0059	0.0033	0.0088	0.0043	...	0.0043	0.0047	...	0.025	0.11	0.0024

[a] $\bar{x}_H(z)$ refers to the mean neutral fraction at redshift z.
[b] FFTT stands for Fast Fourier Transform Telescope, a future square kilometer array optimized for 21 cm tomography as described in [18]. Dipoles in FFTT are all in a giant core, and this configuration does not vary.

imations of these relations. In Sec. IV, we conclude with a discussion of the relative importance of these assumptions, and implications for experimental design.

II. FORECASTING METHODS & ASSUMPTIONS

A. Fundamentals of 21 cm cosmology

1. Power spectrum of 21 cm radiation

We review the basics of the 21 cm radiation temperature and power spectrum only briefly here, and refer the interested reader to [19] for a more comprehensive discussion of the relevant physics. The difference between the observed 21 cm brightness temperature at the redshifted frequency ν and the CMB temperature $T_{\rm CMB}$ is [20]

$$T_b(\mathbf{x}) = \frac{3c^3 h A_{10} n_H(\mathbf{x})[T_S(\mathbf{x}) - T_{\rm CMB}]}{32\pi k_B \nu_0^2 T_S(\mathbf{x})(1+z)^2 (dv_\parallel/dr)}, \quad (1)$$

where T_S is the spin temperature, n_H is the number density of the neutral hydrogen gas, and $A_{10} \approx 2.85 \times 10^{-15}$ s^{-1} is the spontaneous decay rate of 21 cm transition. The factor $dv_\parallel/dr$ is the gradient of the physical velocity along the line of sight (r is the comoving distance), which is $H(z)/(1+z)$ on average (i.e. for no peculiar velocity). Here $H(z)$ is the Hubble parameter at redshift z. The spatially averaged brightness temperature at redshift z is (in units of mK)

$$\bar{T}_b \approx 23.88 \bar{x}_{\rm H} \left(\frac{\bar{T}_S - T_{\rm CMB}}{\bar{T}_S}\right)\left(\frac{\Omega_{\rm b}h^2}{0.02}\right)\left(\frac{0.15}{\Omega_{\rm m}h^2}\frac{1+z}{10}\right)^{1/2}, \quad (2)$$

where $\bar{x}_{\rm H}$ is the mean neutral fraction and $\bar{T}_S$ is the averaged spin temperature. If $T_S \gg T_{\rm CMB}$ in the EoR, the 21 cm emission should therefore be observed at the level of milli-Kelvins.

To calculate the fluctuations, we rewrite Eq. (1) in terms of δ (the hydrogen mass density fluctuation), δ_x (the fluctuation in the ionized fraction), and the gradient of the peculiar velocity $\partial v_r/\partial r$ along the line of sight, using the fact that $dv_\parallel/dr = H(z)/(1+z) + \partial v_r/\partial r$:

$$T_b(\mathbf{x}) = \tilde{T}_b[1 - \bar{x}_{\rm i}(1+\delta_x)](1+\delta)\left(1 - \frac{1}{Ha}\frac{\partial v_r}{\partial r}\right) \times \left(\frac{T_S - T_{\rm CMB}}{T_S}\right). \quad (3)$$

Here $\bar{x}_{\rm i} \equiv 1 - \bar{x}_{\rm H}$ is the mean ionized fraction, and we have defined $\tilde{T}_b \equiv \bar{T}_b/\bar{x}_{\rm H} \times [\bar{T}_S/(\bar{T}_S - T_{\rm CMB})]$. We write $\delta_v \equiv (Ha)^{-1}\partial v_r/\partial r$. In Fourier space, it is straightforward to show that, as long as $\delta \ll 1$ so that linear perturbation theory is valid, $\delta_v(\mathbf{k}) = -\mu^2\delta$, where $\mu = \hat{\mathbf{k}}\cdot\hat{\mathbf{n}}$ is the cosine of the angle between the Fourier vector $\mathbf{k}$ and the line of sight. In this paper, we restrict our attention to the linear regime. We will also, throughout this paper, assume $T_S \gg T_{\rm CMB}$ during the EoR, making the last factor in Eq. (3) unity for the reasons detailed in Sec. I.

In Fourier space, the power spectrum $P_{\Delta T}(\mathbf{k})$ of the 21 cm fluctuations is defined by $\langle \Delta T_b^*(\mathbf{k}) \Delta T_b(\mathbf{k}')\rangle \equiv (2\pi)^3 \delta^3(\mathbf{k} - \mathbf{k}') P_{\Delta T}(\mathbf{k})$, where ΔT_b is the deviation from the mean brightness temperature. It is straightforward to show from Eq. (3) that, to leading order,

$$P_{\Delta T}(\mathbf{k}) = \tilde{T}_b^2\{[\bar{x}_{\rm H}^2 P_{\delta\delta} - 2\bar{x}_{\rm H} P_{{\rm x}\delta} + P_{\rm xx}] + 2\mu^2[\bar{x}_{\rm H}^2 P_{\delta\delta} - \bar{x}_{\rm H} P_{{\rm x}\delta}] + \mu^4 \bar{x}_{\rm H}^2 P_{\delta\delta}\}. \quad (4)$$

Here $P_{\rm xx} = \bar{x}_{\rm i}^2 P_{\delta_x\delta_x}$ and $P_{{\rm x}\delta} = \bar{x}_{\rm i} P_{\delta_x\delta}$ are the ionization power spectrum and the density-ionization power spectrum, respectively. For convenience, we define $\mathcal{P}_{\delta\delta}(k) \equiv \tilde{T}_b^2 \bar{x}_{\rm H}^2 P_{\delta\delta}(k)$, $\mathcal{P}_{x\delta}(k) \equiv \tilde{T}_b^2 \bar{x}_{\rm H} P_{x\delta}(k)$, and $\mathcal{P}_{xx}(k) \equiv \tilde{T}_b^2 P_{\rm xx}(k)$, so the total 21 cm power spectrum can be written as three terms with different angular dependence:

$$P_{\Delta T}(\mathbf{k}) = P_{\mu^0}(k) + P_{\mu^2}(k)\mu^2 + P_{\mu^4}(k)\mu^4, \quad (5)$$

where

$$P_{\mu^0} = \mathcal{P}_{\delta\delta} - 2\mathcal{P}_{x\delta} + \mathcal{P}_{xx}, \quad (6)$$

$$P_{\mu^2} = 2(\mathcal{P}_{\delta\delta} - \mathcal{P}_{x\delta}), \quad (7)$$

$$P_{\mu^4} = \mathcal{P}_{\delta\delta}. \quad (8)$$

Since P_{μ^4} involves only the matter power spectrum that depends only on cosmology, Barkana and Loeb [21,22] argued that, in principle, one can separate cosmology from astrophysical "contaminants" such as $\mathcal{P}_{xx}$ and $\mathcal{P}_{x\delta}$ whose physics is hitherto far from known. We will quantify the accuracy of this conservative approach (which corresponds to our PESS scenario for ionization power spectrum modeling below) in Sec. III.

2. From u to k

The power spectrum $P_{\Delta T}(\mathbf{k})$ and the comoving vector $\mathbf{k}$ (the Fourier dual of the comoving position vector $\mathbf{r}$) are not directly measured by 21 cm experiments. An experiment cannot directly determine which position vector $\mathbf{r}$ a signal is coming from, but instead which vector $\mathbf{\Theta} \equiv \theta_x\hat{e}_x + \theta_y\hat{e}_y + \Delta f \hat{e}_z$ it is coming from, where (θ_x, θ_y) give the angular location on the sky plane and Δf is the frequency difference from the central redshift of a z bin. For simplicity, we assume that the sky volume observed is small enough that we can linearize the relation between $\mathbf{\Theta}$ and $\mathbf{r}$. Specifically, we assume that the sky patch observed is much less than a radian across, so that we can approximate the sky as flat,[1] and that separations in frequency near

[1]The FFTT is designed for all-sky mapping (i.e. the field of view is of order 2π). However, since the angular scales from which we get essentially all our cosmological information are much smaller than a radian (with most information being on arcminute scales), the flat-sky approximation is accurate as long as the data are analyzed separately in many small patches and the constraints are subsequently combined.

the mean redshift z_* are approximately proportional to separations in comoving distance. In these approximations, if there are no peculiar velocities,

$$\boldsymbol{\Theta}_\perp = \frac{\mathbf{r}_\perp}{d_A(z_*)}, \tag{9}$$

$$\Delta f = \frac{\Delta r_\parallel}{y(z_*)}. \tag{10}$$

Here " $\perp$ " denotes the vector component perpendicular to the line of sight, i.e., in the (x, y) plane, and d_A is the comoving angular diameter distance given by [23]

$$d_A(z) = \frac{c}{H_0}|\Omega_k|^{-1/2} S\left[|\Omega_k|^{1/2}\int_0^z \frac{dz'}{E(z')}\right], \tag{11}$$

where

$$E(z) \equiv \frac{H(z)}{H_0} = \sqrt{\Omega_{\rm m}(1+z)^3 + \Omega_{\rm k}(1+z)^2 + \Omega_\Lambda}, \tag{12}$$

is the relative cosmic expansion rate and the function $S(x)$ equals $\sin(x)$ if $\Omega_{\rm k} < 0$, x if $\Omega_{\rm k} = 0$, and $\sinh x$ if $\Omega_{\rm k} > 0$. The conversion factor between comoving distance intervals and frequency intervals is

$$y(z) = \frac{\lambda_{21}(1+z)^2}{H_0 E(z)}, \tag{13}$$

where $\lambda_{21} \approx 21$ cm is the rest-frame wavelength of the 21 cm line.

We write the Fourier dual of $\boldsymbol{\Theta}$ as $\mathbf{u} \equiv u_x\hat{e}_x + u_y\hat{e}_y + u_\parallel\hat{e}_z$ ($u_\parallel$ has units of time). The relation between $\mathbf{u}$ and $\mathbf{k}$ is therefore

$$\mathbf{u}_\perp = d_A\mathbf{k}_\perp, \tag{14}$$

$$u_\parallel = yk_\parallel. \tag{15}$$

In $\mathbf{u}$ space, the power spectrum $P_{\Delta T}(\mathbf{u})$ of 21 cm signals is defined by $\langle\Delta\tilde{T}_b^*(\mathbf{u})\Delta\tilde{T}_b(\mathbf{u}')\rangle = (2\pi)^3\delta^{(3)}(\mathbf{u}-\mathbf{u}')P_{\Delta T}(\mathbf{u})$, and is therefore related to $P_{\Delta T}(\mathbf{k})$ by

$$P_{\Delta T}(\mathbf{u}) = \frac{1}{d_A^2 y}P_{\Delta T}(\mathbf{k}). \tag{16}$$

Note that cosmological parameters affect $P_{\Delta T}(\mathbf{u})$ in two ways: they both change $P_{\Delta T}(\mathbf{k})$ and alter the geometric projection from $\mathbf{k}$ space to $\mathbf{u}$ space. If d_A and y changed while $P_{\Delta T}(\mathbf{k})$ remained fixed, the observable power spectrum $P_{\Delta T}(\mathbf{u})$ would be dilated in both the $\mathbf{u}_\perp$ and $u_\parallel$ directions and rescaled in amplitude, while retaining its shape. Since both d_A and y depend on the three parameters $(\Omega_{\rm k}, \Omega_\Lambda, h)$, and the Hubble parameter is in turn given by the parameters in Table II via the identity $h = \sqrt{\Omega_m h^2/(1-\Omega_\Lambda-\Omega_{\rm k})}$, we see that these geometric effects provide information only about our parameters $(\Omega_{\rm k}, \Omega_\Lambda, \Omega_m h^2)$. Baryon acoustic oscillations in the power spectrum provide a powerful "standard ruler," and the equations above show that if one generalizes to the dark energy to make Ω_Λ an arbitrary function of z, then the cosmic expansion history $H(z)$ can be measured separately at each redshift bin, as explored in [4,24,25]. The 21 cm tomography information on our other cosmological parameters ($n_{\rm s}$, $A_{\rm s}$, $\Omega_b h^2$, m_ν, α, etc.) thus comes only from their direct effect on $P_{\Delta T}(\mathbf{k})$. Also note that $(\Omega_{\rm k}, \Omega_\Lambda)$ affect $P_{\Delta T}(\mathbf{k})$ only by modulating the rate of linear perturbation growth, so they alter only the amplitude and not the shape of $P_{\Delta T}(\mathbf{k})$.

If we were to use Eq. (16) to infer $P_{\Delta T}(\mathbf{k})$ from the measured power spectrum $P_{\Delta T}(\mathbf{u})$ while assuming incorrect cosmological parameter values, then this geometric scaling would cause the inferred $P_{\Delta T}(\mathbf{k})$ to be distorted by the so-called Alcock-Paczyński (AP) effect [26,27] and not take the simple form of Eqs. (5)–(8). To avoid this complication, we therefore perform our Fisher matrix analysis directly in terms of $P_{\Delta T}(\mathbf{u})$, since this quantity is directly measurable without any cosmological assumptions.

The above transformations between $\mathbf{u}$ space and $\mathbf{r}$ space are valid when there are no peculiar velocities. The radial peculiar velocities v_r that are present in the real world induce the familiar redshift space distortions that were discussed in Sec. II A 1, causing μ^2 and μ^4 power spectrum anisotropies that were described there.

B. Assumptions about $\mathcal{P}_{xx}$ and $\mathcal{P}_{x\delta}$

During the EoR, ionized bubbles (HII regions) in the IGM grow and eventually merge with one another. Consequently, $\mathcal{P}_{xx}$(k) and $\mathcal{P}_{x\delta}$(k) contribute significantly to the total 21 cm power spectrum. The study of the forms of these two ionization power spectra has made rapid progress recently, particularly through the semianalytical calculations [14,16,28,29] and radiative transfer simulations [30,31]. However, these models depend on theoretically presumed parameters whose values cannot currently be calculated from first principles. From the experimental point of view, it is therefore important to develop data analysis methods that depend only on the most generic features of the ionization power spectra. In this paper, we consider three methods—our OPT, MID, and PESS models—that model $\mathcal{P}_{xx}$ and $\mathcal{P}_{x\delta}$ as follows:

$$\text{(OPT)} \quad \begin{cases} \mathcal{P}_{xx}(k) &= 0, \\ \mathcal{P}_{x\delta}(k) &= 0, \end{cases} \tag{17}$$

$$\text{(MID)} \quad \begin{cases} \mathcal{P}_{xx}(k) = b_{\rm xx}^2[1+\alpha_{\rm xx}(kR_{\rm xx})+(kR_{\rm xx})^2]^{-(\gamma_{\rm xx}/2)}\mathcal{P}_{\delta\delta}^{\rm (fid)}, \\ \mathcal{P}_{x\delta}(k) = b_{\rm x\delta}^2\exp[-\alpha_{\rm x\delta}(kR_{\rm x\delta})-(kR_{\rm x\delta})^2]\mathcal{P}_{\delta\delta}^{\rm (fid)}, \end{cases} \tag{18}$$

$$\text{(PESS)} \quad \begin{cases} \mathcal{P}_{xx}(k) = \text{arbitrary}, \\ \mathcal{P}_{x\delta}(k) = \text{arbitrary}. \end{cases} \tag{19}$$

In the next three subsections, we explain these models in turn.

1. OPT model

It is likely that before reionization started (while $\bar{x}_{\rm H} = 1$ and $\mathcal{P}_{xx} = \mathcal{P}_{x\delta} = 0$), hydrogen gas had already been sufficiently heated such that $T_S \gg T_{\rm CMB}$. In this regime, Eq. (17) holds. This OPT scenario is clearly the simplest model, since the total 21 cm power spectrum is simply proportional to $\mathcal{P}_{\delta\delta}$: $P_{\Delta T}(\mathbf{k}) = \mathcal{P}_{\delta\delta}(k)(1+\mu^2)^2$. To forecast the 1σ error, we use the Fisher matrix formalism [32]. Repeating the derivation in [33], the Fisher matrix for cosmological parameters λ_a ($a = 1, \ldots, N_p$) is

$$\mathbf{F}_{ab} = \frac{1}{2}\int\left(\frac{\partial \ln P^{\rm tot}_{\Delta T}(\mathbf{u})}{\partial \lambda_a}\right)\left(\frac{\partial \ln P^{\rm tot}_{\Delta T}(\mathbf{u})}{\partial \lambda_b}\right) V_\Theta \frac{d^3u}{(2\pi)^3}, \quad (20)$$

where the integral is taken over the observed part of $\mathbf{u}$ space, and $P^{\rm tot}_{\Delta T}(\mathbf{u})$ denotes the combined power spectrum from cosmological signal and all forms of noise. Here $V_\Theta = \Omega \times B$ is the volume of the $\mathbf{\Theta}$ space where Ω is the solid angle within the field of view and B is the frequency size of a z bin. The Fisher matrix determines the parameter errors as $\Delta\lambda_a = \sqrt{(\mathbf{F}^{-1})_{aa}}$.

For computational convenience, we subdivide u space into pixels so small that the power spectrum is roughly constant in each one, obtaining

$$\mathbf{F}_{ab} \approx \sum_{\rm pixels} \frac{1}{[\delta P_{\Delta T}(\mathbf{u})]^2}\left(\frac{\partial P_{\Delta T}(\mathbf{u})}{\partial \lambda_a}\right)\left(\frac{\partial P_{\Delta T}(\mathbf{u})}{\partial \lambda_b}\right), \quad (21)$$

where the power spectrum measurement error in a pixel at $\mathbf{u}$ is

$$\delta P_{\Delta T}(\mathbf{u}) = \frac{P^{\rm tot}_{\Delta T}(\mathbf{u})}{N_c^{1/2}} = \frac{P_{\Delta T}(\mathbf{u}) + P_N(u_\perp)}{N_c^{1/2}}. \quad (22)$$

Here $P_N(u_\perp)$ is the noise power spectrum and will be discussed in detail in Sec. II G 3; note that it is independent of $u_\parallel$ and depends only on $u_\perp$ through the baseline distribution of the antenna array.

$$N_c = 2\pi k^2 \sin\theta \Delta k \Delta\theta \times {\rm Vol}/(2\pi)^3 \quad (23)$$

is the number of independent cells in an annulus summing over the azimuthal angle. We have the factor $\sqrt{1/N_c}$ in $\delta P_{\Delta T}$ instead of the normal $\sqrt{2/N_c}$ because we only sum over half the sphere.

2. MID model

After reionization starts, both ionization power spectra $\mathcal{P}_{xx}$ and $\mathcal{P}_{x\delta}$ make significant contributions to the total 21 cm power spectrum. We explore two different analysis methods—our MID and PESS models—for separating the cosmological signal from these astrophysical contaminants (i.e. $\mathcal{P}_{xx}$ and $\mathcal{P}_{x\delta}$).

Our MID model assumes that both ionization power spectra $\mathcal{P}_{xx}(k)$ and $\mathcal{P}_{x\delta}(k)$ are smooth functions of k which can be parametrized by a small number of nuisance parameters $\beta_1, \ldots, \beta_{n_{\rm ion}}$ related to reionization physics. Combining these ionization parameters with our cosmological ones λ_a into a larger parameter set p_α ($\alpha = 1, \ldots, N_p + n_{\rm ion}$), we can jointly constrain them by measuring $P_{\Delta T}(\mathbf{u})$.

In the Appendix we will describe a χ^2 goodness-of-fit test for quantifying whether this parametrization is valid. The Fisher matrix for measuring p_α is simply

$$F_{\alpha\beta} = \sum_{\rm pixels} \frac{1}{[\delta P_{\Delta T}(\mathbf{u})]^2}\frac{\partial P_{\Delta T}(\mathbf{u})}{\partial p_\alpha}\frac{\partial P_{\Delta T}(\mathbf{u})}{\partial p_\beta}. \quad (24)$$

This Fisher matrix $F_{\alpha\beta}$ is not block diagonal; i.e., there are correlations between the cosmological and ionization parameters, reflecting the fact that both affect $\mathcal{P}_{xx}(k)$ and $\mathcal{P}_{x\delta}(k)$. The inversion of the Fisher matrix therefore leads to the degradation of the constraints of cosmological parameters. However, the total 21 cm power spectrum is usually smaller in magnitude in the MID model than in the OPT model [see Eq. (4)], giving less sample variance. This means that as long as noise in a 21 cm experiment dominates over sample variance, the MID model will give weaker constraints than the OPT model, because of the degeneracies. For future experiments with very low noise, however, it is possible to have the opposite situation, if the reduction in sample variance dominates over the increase in degeneracy. This of course, does not mean that the MID model is more optimistic than the OPT model, merely that the OPT model is assuming an unrealistic power spectrum.

Having set up the general formalism, we now propose a parametrization specified by Eq. (18), with fiducial values of ionization parameters given in Table III. This parametrization was designed to match the results of the radiative transfer simulations in model I of [30], and Fig. 2 shows that the fit is rather good in the range $k = 0.1$–2 Mpc^{-1} to

TABLE III. Fiducial values of ionization parameters adopted for Fig. 2. $R_{\rm xx}$ and $R_{\rm x\delta}$ are in units of Mpc, while other parameters are unitless.

z	$\bar{x}_{\rm H}$	$b^2_{\rm xx}$	$R_{\rm xx}$	$\alpha_{\rm xx}$	$\gamma_{\rm xx}$	$b^2_{\rm x\delta}$	$R_{\rm x\delta}$	$\alpha_{\rm x\delta}$
9.2	0.9	0.208	1.24	−1.63	0.38	0.45	0.56	−0.4
8.0	0.7	2.12	1.63	−0.1	1.35	1.47	0.62	0.46
7.5	0.5	9.9	1.3	1.6	2.3	3.1	0.58	2
7.0	0.3	77	3.0	4.5	2.05	8.2	0.143	28

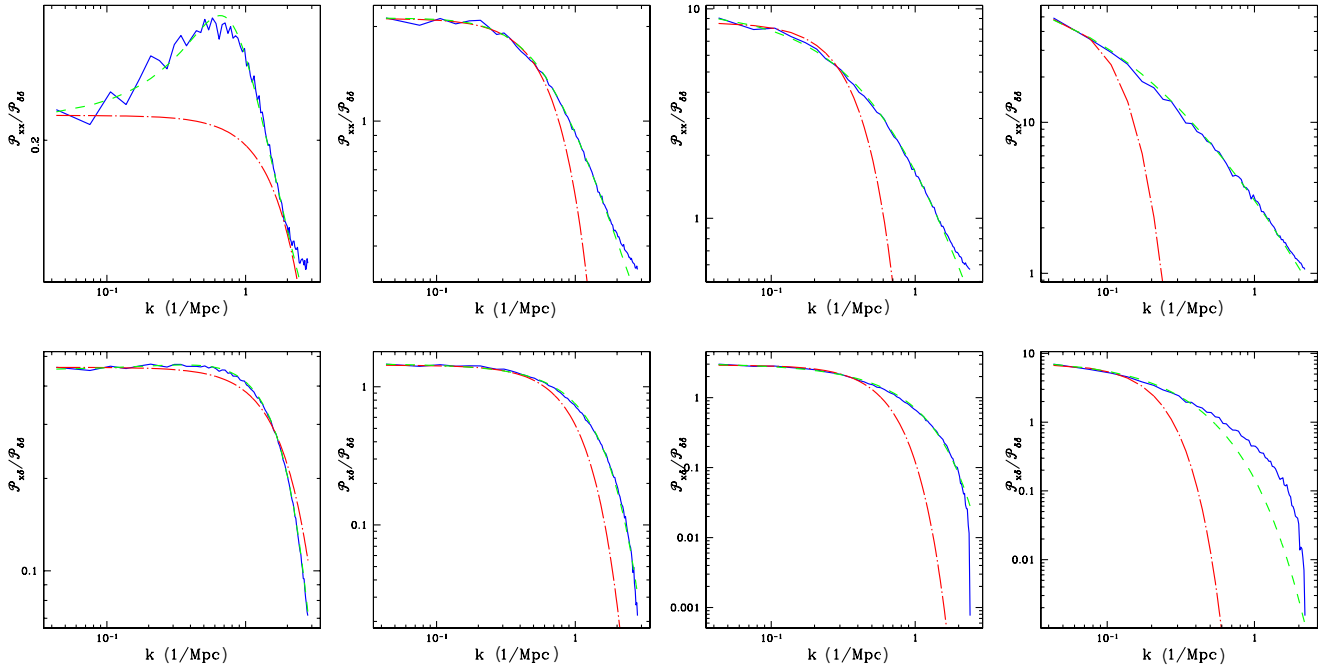

FIG. 2 (color online). Fits to the ionization power spectra at several redshifts. Solid (blue) lines are the results of the radiative transfer simulation in model I of the McQuinn *et al.* paper [30]. Dashed (green) lines are fitting curves of our parametrization. Dot-dashed (red) lines are best fits using the parametrization suggested by Santos and Cooray [3]. Top panels: $\mathcal{P}_{xx}/\mathcal{P}_{\delta\delta} = P_{\rm xx}/(\bar{x}_{\rm H}^2 P_{\delta\delta})$. Bottom panels: $\mathcal{P}_{x\delta}/\mathcal{P}_{\delta\delta} = P_{\rm x\delta}/(\bar{x}_{\rm H} P_{\delta\delta})$. From left to right: $z = 9.2$, 8.0, 7.5, 7.0 ($\bar{x}_{\rm i} = 0.10$, 0.30, 0.50, 0.70, respectively).

which the 21 cm experiments we consider are most sensitive.

The radiative transfer simulations implemented in [30] are post-processed on top of a 1024^3 N-body simulation in a box of size 186 Mpc. Three models for the reionization history are considered in [30]:

(1) In model I, all dark matter halos above $m_{\rm cool}$ (corresponding to the minimum mass galaxy in which the gas can cool by atomic transitions and form stars, e.g. $m_{\rm cool} \approx 10^8 M_\odot$ at $z = 8$) contribute ionizing photons at a rate that is proportional to their mass.

(2) In model II, the ionizing luminosity of the sources scales as halo mass to the 5/3 power; i.e. more massive halos dominate the production of ionizing photons than in model I.

(3) In model III, which has the same source parametrization as in model I except for doubled luminosity, minihalos with $m > 10^5 M_\odot$ absorb incident ionizing photons out to their virial radius unless they are photo-evaporated (but do not contribute ionizing photons).

It appears to be a generic feature in the simulation results that the ratios of functions at large k fall off like a power law for $\mathcal{P}_{xx}(k)/\mathcal{P}_{\delta\delta}(k)$, and exponentially for $\mathcal{P}_{x\delta}(k)/\mathcal{P}_{\delta\delta}(k)$. At small k, $\mathcal{P}_{xx}(k)/\mathcal{P}_{\delta\delta}(k)$ can either increase or decrease approximately linearly as k increases, while $\mathcal{P}_{x\delta}(k)/\mathcal{P}_{\delta\delta}(k)$ is asymptotically constant. Our parametrization in Eq. (18) captures these features: at large k, $\mathcal{P}_{xx}(k)/\mathcal{P}_{\delta\delta}(k) \propto k^{-\gamma_{\rm xx}}$ and $\mathcal{P}_{x\delta}(k)/\mathcal{P}_{\delta\delta}(k) \propto \exp(-(kR_{\rm x\delta})^2)$; at small k, $\mathcal{P}_{xx}(k)/\mathcal{P}_{\delta\delta}(k) \propto (1 - (\gamma_{\rm xx}\alpha_{\rm xx}R_{\rm xx}/2)k)$ and $\mathcal{P}_{x\delta}(k)/\mathcal{P}_{\delta\delta}(k) \propto (1 - \alpha_{\rm x\delta}R_{\rm x\delta}k)$ (both $\alpha_{\rm xx}$ and $\alpha_{\rm x\delta}$ can be either positive or negative). Figure 2 also shows that for $P_{\rm xx}(k)$ and also for $P_{\rm x\delta}(k)$ at large k, our parametrization further improves over the parametrization $P(k)/P_{\delta\delta} = b^2 e^{-(kR)^2}$ suggested by Santos and Cooray [3], which works well for $P_{\rm x\delta}(k)$ at small k.

To be conservative, we discard cosmological information from $\mathcal{P}_{x\delta}(k)$ and $\mathcal{P}_{xx}(k)$ in our Fisher matrix analysis by using the fiducial power spectrum $\mathcal{P}_{\delta\delta}(k)^{\rm (fid)}$ rather than the actual one $\mathcal{P}_{\delta\delta}(k)$ in Eq. (18). This means that the derivatives of $\mathcal{P}_{x\delta}(k)$ and $\mathcal{P}_{xx}(k)$ with respect to the cosmological parameters vanish in Eq. (24). It is likely that we can do better in the future: once the relation between the ionization power spectra and the matter power spectrum can be reliably calculated either analytically or numerically, the ionization power spectra can contribute to further constraining cosmology.

In addition to the fit of model I shown in Fig. 2, we also fit our model (with different fiducial values from those listed in Table III) to the simulations using models II and III in [30], and find that the parametrization is flexible enough to provide good fits to all three simulations, suggesting that the parametrization in Eq. (18) may be generically valid and independent of models. Note, however, that at low redshifts ($\bar{x}_{\rm i} \gtrsim 0.7$), our parametrization of $\mathcal{P}_{x\delta}/\mathcal{P}_{\delta\delta}$ does not work well at large k, in that the simulation falls off less rapidly than exponentially. This may be because when HII regions dominate the IGM, the ionized

bubbles overlap in complicated patterns and correlate extremely nonlinearly at small scales. This partial incompatibility indicates that our parametrization [i.e. Eq. (18)] is only accurate for small $\bar{x}_i$, i.e. before nonlinear ionization patterns come into play.

In the remainder of this paper, we will adopt the values in Table III as fiducial values of the ionization parameters.

3. PESS model

By parametrizing the ionization power spectra with a small number of constants, the MID model rests on our understanding of the physics of reionization. From the point of view of a maximally cautious experimentalist, however, constraints on cosmological parameters should not depend on how well one models reionization. In this spirit, Barkana and Loeb [21,22] proposed what we adopt as our "PESS" model for separating the physics $\mathcal{P}_{\delta\delta}(k)$ from the "gastrophysics" $\mathcal{P}_{xx}(k)$ and $\mathcal{P}_{x\delta}(k)$. Instead of assuming a specific parametrization, the PESS model makes no *a priori* assumptions about the ionization power spectra. In each k bin that contains more than three pixels in $\mathbf{u}$ space, one can, in principle, separate $P_{\mu^4}(k) = \mathcal{P}_{\delta\delta}(k)$ from the other two moments. The PESS model essentially only constrains cosmology from the P_{μ^4} term and therefore loses all information in P_{μ^0} and P_{μ^2}. We now set up the Fisher matrix formalism for the PESS model that takes advantage of the anisotropy in $P_{\Delta T}(\mathbf{k})$ arising from the velocity field effect. Numerical evaluations will be performed in Sec. III A.

The observable in 21 cm tomography is the brightness temperature $T_b(\mathbf{x})$. In Fourier space, the covariance matrix between two pixels $\mathbf{k}_i$ and $\mathbf{k}_j$ is $\mathbf{C}_{ij} = \delta_{ij}[P_{\Delta T}(\mathbf{k}_i) + P_N(k_\perp)]$, assuming that the measurements in two different pixels are uncorrelated.[2] The total 21 cm power spectrum is $P_{\Delta T}(\mathbf{k}) = P_{\mu^0}(k) + P_{\mu^2}(k)\mu^2 + P_{\mu^4}(k)\mu^4$. For convenience, we use the shorthand notation P_A, where $P_1 \equiv P_{\mu^0}$, $P_2 \equiv P_{\mu^2}$, and $P_3 \equiv P_{\mu^4}$, and define the $a_A = 0, 2, 4$ for $A = 1, 2, 3$, respectively. Thus the power spectrum can be rewritten as $P_{\Delta T} = \sum_{A=1}^{3} P_A \mu^{a_A}$. Treating $P_A(k)$ at each k bin as parameters, the derivatives of the covariance matrix are simply $\partial \mathbf{C}_{ij}/\partial P_A(k) = \delta_{ij}\mu^{a_A}$, where $|\mathbf{k}_i|$ resides in the shell of radius k with width Δk. Since the different k bins all decouple, the Fisher matrix for measuring the moments $P_A(k)$ is simply a separate 3×3 matrix for each k bin:

$$F_{AA'}(k) = \frac{1}{2}\,\mathrm{tr}\left[\mathbf{C}^{-1}\frac{\partial \mathbf{C}}{\partial P_A(k)}\mathbf{C}^{-1}\frac{\partial \mathbf{C}}{\partial P_{A'}(k)}\right] = \sum_{\text{upper half-shell}} \frac{\mu^{a_A + a_{A'}}}{[\delta P_{\Delta T}(\mathbf{k})]^2}, \tag{25}$$

[2]We ignore here a δ function centered at the origin since 21 cm experiments will not measure any $k = 0$ modes.

where $\delta P_{\Delta T}(\mathbf{k}) = N_c^{-1/2}[P_{\Delta T}(\mathbf{k}) + P_N(k_\perp)]$. Here $P_N(k_\perp)$ is related to $P_N(u_\perp)$ by Eq. (16). Again the sum is over the upper half of the spherical shell $k < |\mathbf{k}| < k + \Delta k$. The 1σ error of $P_3 = P_{\mu^4}$ is $\delta P_3(k) = \sqrt{F^{-1}{}_{33}(k)}$. Once $\mathcal{P}_{\delta\delta} = P_{\mu^4}$ is separated from other moments, $\mathcal{P}_{\delta\delta}$ can be used to constrain cosmological parameters λ_a with the Fisher matrix as given in Eq. (21).

We have hitherto discussed the anisotropy in $P_{\Delta T}(\mathbf{k})$ that arises from the velocity field effect. However, the AP effect may further contribute to the anisotropy in that it creates a μ^6 dependence and modifies the μ^4 term [26,27]. The AP effect can be distinguished from the velocity field effect since the P_{μ^6} term is unique to the AP effect. Thus, one can constrain cosmological parameters from P_{μ^4} and P_{μ^6} [2], involving the inversion of a 4×4 matrix which loses even more information and therefore further weakens constraints. Therefore, the PESS Fisher matrix that we have derived without taking the AP effect into account can be viewed as an upper bound on how well the PESS approach can do in terms of cosmological parameter constraints. However, this maximally conservative 4×4 matrix approach may be inappropriately pessimistic, since the AP-induced clustering anisotropy is typically very small within the observationally allowed cosmological parameter range, whereas the velocity-induced anisotropies can be of order unity.

C. Assumptions about linearity

To avoid fitting to modes where δ_k is nonlinear and physical modeling is less reliable, we impose a sharp cutoff at $k_{\max}$ and exclude all information for $k > k_{\max}$. We take $k_{\max} = 2\ \mathrm{Mpc}^{-1}$ for our MID model, and investigate the $k_{\max}$ dependence of cosmological parameter constraints in Sec. III B.

D. Assumptions about non-Gaussianity

Non-Gaussianity of ionization signals generically becomes important at high $\bar{x}_i$. Using cosmic reionization simulations with a large volume and high resolution, Lidz *et al.* [34] and Santos *et al.* [35] found non-negligible (a factor of 1.5) differences in the full power spectrum at high $\bar{x}_i$ ($\bar{x}_i \gtrsim 0.35$)). To get a rough sense of the impact of non-Gaussianity on cosmological parameter constraints, we simply model it as increasing the sample variance by a factor ξ. We thus write the total power spectrum as

$$\delta P_{\Delta T}(\mathbf{u}) = N_c^{-1/2}[\xi P_{\Delta T}(\mathbf{u}) + P_N(u_\perp)], \tag{26}$$

where ξ is the factor by which the sample variance is increased. The parameter ξ should take the value $\xi \approx 1$ (Gaussian) at epochs with low $\bar{x}_i$ and $1 < \xi \lesssim 2$ (non-Gaussian) at high $\bar{x}_i$.

E. Assumptions about reionization history and redshift range

As illustrated in Fig. 1, 21 cm tomography can probe a wide range of redshifts . However, one clearly cannot simply measure a single power spectrum for the entire volume, as the clustering evolves with cosmic time: The matter power spectrum changes gradually due to the linear growth of perturbations [36]. More importantly, the ionization power spectra vary dramatically with redshift through the epoch of reionization. We incorporate these complications by performing our analysis separately in a series of redshift slices, each chosen to be narrow enough that the matter and ionization power spectra can be approximated as constant in redshift within each slice. This dictates that for a given assumed reionization history, thinner redshift slices must be used around redshifts where $\bar{x}_{\rm H}$ varies dramatically.

In this paper, we will consider two rather opposite toy models in Sec. III:

(i) OPT: A sharp reionization that begins and finishes at one redshift (say $z \lesssim 7$).

(ii) MID/PESS: A gradual reionization that spans a range of redshifts, assuming the ionization parameter values that fit model I simulation of the McQuinn *et al.* paper [30].

For the latter scenario, the ionization fraction $\bar{x}_{\rm H}$ is not a linear function of redshift. For example, in the simulation of McQuinn *et al.* [30], $\bar{x}_{\rm H} = 0.9$, 0.7, 0.5, and 0.3 correspond to redshifts $z = 9.2$, 8.0, 7.5, and 7.0, respectively. For our different scenarios, we therefore adopt the redshift ranges $6.8 < z < 10$ that are divided into four redshift slices centered at the above redshifts (OPT), $6.8 < z < 8.2$ split into three bins centered at $z = 7.0$, 7.5, and 8.0 (MID), and $7.3 < z < 8.2$ split into two slices centered at $z = 7.5$ and 8.0.

F. Assumptions about cosmological parameter space

Since the impact of the choice of cosmological parameter space and related degeneracies has been extensively studied in the literature, we will perform only a basic analysis of this here. We work within the context of standard inflationary cosmology with adiabatic perturbations, and parametrize cosmological models in terms of 12 parameters (see, e.g., Table II in [37] for explicit definitions) whose fiducial values are assumed as follows: $\Omega_{\rm k} = 0$ (spatial curvature), $\Omega_\Lambda = 0.7$ (dark energy density), $\Omega_{\rm b} = 0.046$ (baryon density), $h = 0.7$ (Hubble parameter $H_0 \equiv 100h$ km s^{-1} Mpc^{-1}), $\tau = 0.1$ (reionization optical depth), $\Omega_\nu = 0.0175$ (massive neutrino density), $n_{\rm s} = 0.95$ (scalar spectral index), $A_s = 0.83$ (scalar fluctuation amplitude), $r = 0$ (tensor-to-scalar ratio), $\alpha = 0$ (running of spectral index), $n_t = 0$ (tensor spectral index), and $w = -1$ (dark energy equation of state). We will frequently use the term "vanilla" to refer to the minimal model space parametrized by $(\Omega_\Lambda, \Omega_{\rm m}h^2, \Omega_{\rm b}h^2, n_{\rm s}, A_{\rm s}, \tau)$ combined with $\bar{x}_{\rm H}(z)$ and ionization parameters at all observed z bins, setting $\Omega_{\rm k}$, $\Omega_\nu h^2$, r, α, $n_{\rm t}$, and w fixed at their fiducial values.

G. Assumptions about data

The MWA, LOFAR, SKA, and FFTT instruments are still in their planning/design/development stages. In this paper, we adopt the key design parameters from [17] for MWA, [38] and www.skatelescope.org for SKA, www.lofar.org for LOFAR, and [18] for FFTT, unless explicitly stated otherwise.

1. Interferometers

We assume that MWA will have 500 correlated 4 m $\times$ 4 m antenna tiles, each with 16 dipoles. Each individual tile will have an effective collecting area of 14 m^2 at $z = 8$ and 18 m^2 at $z \gtrsim 12$. LOFAR will have 77 large (diameter $\sim$100 m) stations, each with thousands of dipole antennae such that it has the collecting area nearly 50 times larger than each antenna tile of MWA. Each station can simultaneously image N regions in the sky. We set $N = 2$ in this paper but this number may be larger for the real array. The design of SKA has not been finalized. We assume the "smaller antennae" version of SKA, in which SKA will have 7000 small antennae, much like MWA, but each panel will have a much larger collecting area. The FFTT is a future square kilometer array optimized for 21 cm tomography as described in [18]. Unlike the other interferometers we consider, which add in phase the dipoles in each panel or station, the FFTT correlates all of its dipoles, resulting in more information. We evaluate the case where the FFTT contains a million 1 m $\times$ 1 m dipole antennae in a contiguous core subtending a square kilometer, providing a field of view of 2π steradians.

For all interferometers, we assume that the collecting area $A_e \propto \lambda^2$, like a simple dipole, except that A_e is saturated at $z \sim 12$ in MWA since the wavelength $\lambda = 21(1 + z)$ cm exceeds the physical radius of an MWA antenna panel. The summary of the detailed specifications adopted in this paper is listed in Table IV.

2. Configuration

The planned configurations of the above-mentioned interferometers are quite varied. However, all involve some combination of the following elements, which we will explore in our calculations:

(1) A *nucleus* of radius R_0 within which the area coverage fraction is close to 100%.

(2) A *core* extending from radius R_0 out to $R_{\rm in}$ where the coverage density drops like some power law r^{-n}.

(3) An *annulus* extending from $R_{\rm in}$ to $R_{\rm out}$ where the coverage density is low but rather uniform.

In its currently planned design, the MWA will have a small nucleus, while the core density falls off as r^{-2} until a sharp

TABLE IV. Specifications for 21 cm interferometers.

Experiment	$N_{\rm ant}$	Minimum baseline (m)	Field of view (deg^2)	A_e (m^2) at $z = 6/8/12$[a]
MWA	500	4	$\pi 16^2$	9/14/18
SKA	7000	10	$\pi 8.6^2$	30/50/104
LOFAR	77	100	$2 \times \pi 2.4^2$	397/656/1369
FFTT	10^6	1	2π	1/1/1

[a]We assume that the effective collecting area is proportional to λ^2 such that the sensitivity ($A_e/T_{\rm sys}$ in m^{2}K^{-1}) meets the design specification.

cutoff at $R_{\rm in}$. For LOFAR we assume 32 stations in the core, and another 32 stations in an outer annulus out to radius $R_{\rm out} \sim 6$ km. For SKA we assume 20% in the core, and 30% in the annulus out to radius $R_{\rm out} \sim 5$ km. We ignore the measurements from any dilute distribution of antenna panels outside $R_{\rm out}$. For LOFAR and SKA, we assume a uniform distribution of antennae in the annulus, but with an inner core profile like that of the MWA, i.e., a nucleus of radius $R_0 = 285/189$ m (LOFAR/SKA) and an r^{-2} falloff outside this compact core. We assume an azimuthally symmetric distribution of baselines in all arrays.

For an array with $N_{\rm in}$ antennae within $R_{\rm in}$, we can define a quantity

$$R_0^{\rm max} \equiv \sqrt{\frac{N_{\rm in}}{\rho_0 \pi}}, \tag{27}$$

where ρ_0 is the area density of the nucleus. $R_0^{\rm max}$ is the maximal radius of the nucleus, corresponding to the case where it contains all the $N_{\rm in}$ antennae and there is no core.

It is also convenient to parametrize the distribution of these $N_{\rm in}$ antennae within $R_{\rm in}$ by two numbers: the fraction η that are in the nucleus and the falloff index n of the core. It is straightforward to show that R_0 and $R_{\rm in}$ are related to η and n by

$$R_0 = \sqrt{\eta} R_0^{\rm max}, \tag{28}$$

$$R_{\rm in} = R_0 \left(\frac{2 - n(1-\eta)}{2\eta}\right)^{1/(2-n)} \tag{29}$$

if $n \neq 2$. The analytic relation for $n = 2$ is $R_{\rm in} = R_0 \exp[(1-\eta)/(2\eta)]$, which can be well approximated in numerical calculation by taking $n = 2 + \epsilon$ in Eq. (29) with $\epsilon \sim 10^{-10}$.

In Sec. III E, we will scan almost all possible design configurations and find the optimal one for constraining cosmology. There are two independent ways to vary array configurations, as illustrated by Fig. 3: by varying R_0 with $R_{\rm in}$ fixed, and by varying $R_{\rm in}$ with R_0 fixed. Contributions from antennae in the annulus are negligible compared to the core, so varying $R_{\rm out}$ is not interesting.

In other parts of Sec. III, we will assume the intermediate configuration $\eta = 0.8$ and $n = 2$ (except for the FFTT which is purely in a giant core) with the planned number of antennae in the core and annulus. Note that this configuration is optimized from the currently planned design.

3. Detector noise

The 21 cm radio interferometers measure visibility $\mathbf{V}$. The visibility for a pair of antennae is defined as [39]

$$\mathbf{V}(u_x, u_y, \Delta f) = \int dx dy \Delta T_b(x, y, \Delta f) e^{-i(u_x x + u_y y)}, \tag{30}$$

where (u_x, u_y) are the number of wavelengths between the antennae. The hydrogen 3D map is the Fourier transform in the frequency direction $\tilde{I}(\mathbf{u}) \equiv \int d\Delta f \mathbf{V}(u_x, u_y, \Delta f) \times \exp(-i\Delta f u_\parallel)$ where $\mathbf{u} = u_x \hat{e}_x + u_y \hat{e}_y + u_\parallel \hat{e}_z$. The detector noise covariance matrix for an interferometer is [2,40]

$$C^N(\mathbf{u}_i, \mathbf{u}_j) = \left(\frac{\lambda^2 B T_{\rm sys}}{A_e}\right)^2 \frac{\delta_{ij}}{B t_{\mathbf{u}_i}}, \tag{31}$$

where B is the frequency bin size, $T_{\rm sys}$ is the system temperature, and $t_{\mathbf{u}} \approx (A_e t_0/\lambda^2) n(u_\perp)$ is the observation time for the visibility at $|\mathbf{u}_\perp| = d_A |\mathbf{k}| \sin\theta$. Here t_0 is the total observation time, and n is the number of baselines in an observing cell.

The covariance matrix of the 21 cm signal $\tilde{I}(\mathbf{u})$ is related to the power spectrum $P_{\Delta T}(\mathbf{k})$ by [2]

$$C^{\rm SV}(\mathbf{u}_i, \mathbf{u}_j) \equiv \langle \tilde{I}^*(\mathbf{u}_i) \tilde{I}(\mathbf{u}_j) \rangle = P_{\Delta T}(\mathbf{u}_i) \frac{\lambda^2 B}{A_e} \delta_{ij}. \tag{32}$$

Therefore, the noise in the power spectrum is

$$P^N(u_\perp) = \left(\frac{\lambda^2 T_{\rm sys}}{A_e}\right)^2 \frac{1}{t_0 n(u_\perp)}. \tag{33}$$

For all interferometers, the system temperature is dominated by sky temperature $T_{\rm sky} \approx 60(\lambda/1\ {\rm m})^{2.55}$ K due to synchrotron radiation in reasonably clean parts of the sky. Following [17], we set $T_{\rm sys} = 440$ K at $z = 8$ and $T_{\rm sys} = 690$ K at $z = 10$.

H. Assumptions about residual foregrounds

There have been a number of papers discussing foreground removal for 21 cm tomography (e.g. [41–44] and references therein), and much work remains to be done on this important subject, as the amplitudes of residual foregrounds depend strongly on cleaning techniques and as-

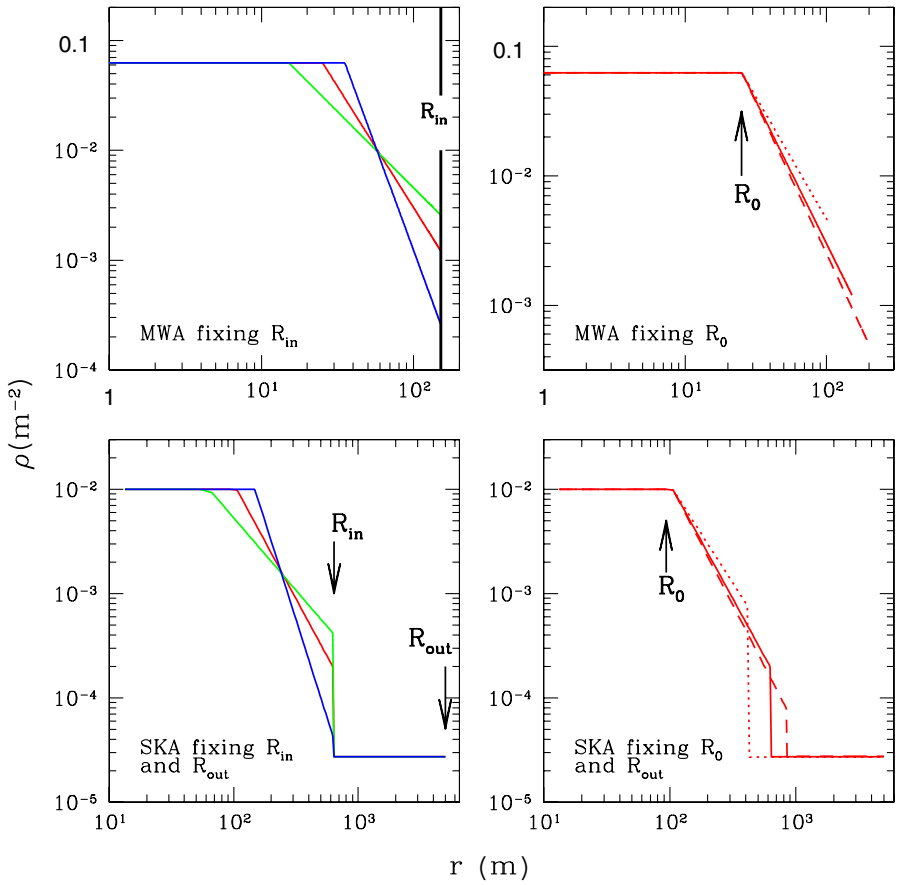

FIG. 3 (color online). Examples of array configuration changes. For MWA (upper panels), antennae are uniformly distributed inside the nucleus radius R_0, and the density ρ falls off like a power law for $R_0 < r < R_{\rm in}$, where $R_{\rm in}$ is the core radius. For SKA (lower panels) and similarly for LOFAR, there is, in addition, a uniform yet dilute distribution of antennae in the annulus $R_{\rm in} < r < R_{\rm out}$, where $R_{\rm out}$ is the outer annulus radius. When R_0 is decreased ($R_0 = 0.7/0.5/0.3 \times R_0^{\rm max}$) with $R_{\rm in} = 3.0 \times R_0^{\rm max}$ fixed (left panels), the density in the core falls off more slowly (blue/red/green curves). When $R_{\rm in}$ is decreased ($R_{\rm in} = 4.0/3.0/2.0 \times R_0^{\rm max}$) with $R_0 = 0.5 \times R_0^{\rm max}$ fixed (right panels), the density in the core also falls off less steeply (dashed/solid/dotted curves).

sumptions, and can potentially dominate the cosmological signal. The work of Wang *et al.* [41] and McQuinn *et al.* [2] suggested that after fitting out a low-order polynomial from the frequency dependence in each pixel, the residual foregrounds were negligible for $k > 2\pi/yB$, where yB is the comoving width of a z bin. To obtain a crude indication of the impact of residual foregrounds, we therefore adopt the rough approximation that all data below some cutoff value $k_{\rm min}$ are destroyed by foregrounds while the remainder have negligible contamination. We choose $k_{\rm min} = (1/2/4) \times \pi/yB$ for the OPT/MID/PESS scenarios, and also explore wider ranges below.

III. RESULTS AND DISCUSSION

In this section, we numerically evaluate how the accuracy of cosmological parameter constraints depends on the various assumptions listed above. Where possible, we attempt to provide intuition for these dependences with simple analytical approximations. In most cases, we explore the dependence on one assumption at a time by evaluating the PESS, MID, and OPT scenarios for this assumption while keeping all other assumptions fixed to the baseline MID scenario.

A. Varying ionization power spectrum modeling and reionization histories

1. Basic results

We start by testing assumptions in the ionization power modeling of $P_{\rm xx}$ and $P_{{\rm x}\delta}$. In Table V we show the accuracy with which the 21 cm power spectrum can place constraints on the cosmological parameters from three z bins ranging from $z = 6.8$–8.2. We fix the assumptions concerning $k_{\rm max}$, the foreground removal, and the array layout and specifications, but vary the sophistication with which we model the ionization power.

Our results agree with those of previous studies [1,2]; i.e. 21 cm data alone (except for the optimized FFTT) cannot place constraints comparable with those from Planck CMB data. However, if 21 cm data are combined with CMB data, the parameter degeneracies can be broken, yielding strin-

TABLE V. How cosmological constraints depend on the ionization power spectrum modeling and reionization history. We assume observations of 4000 hours on two places in the sky in the range of $z = 6.8$–8.2 that is divided into three z bins centered at $z = 7.0$, 7.5, and 8.0, respectively, $k_{\rm max} = 2\ {\rm Mpc}^{-1}$, $k_{\rm min} = 2\pi/yB$, and a quasigiant core configuration (except for FFTT which is a giant core). The 1σ errors of ionization parameters in the MID model, marginalized over other vanilla parameters, are listed separately in Table VI.

		Vanilla alone											
	Model	$\Delta\Omega_\Lambda$	$\Delta\ln(\Omega_m h^2)$	$\Delta\ln(\Omega_b h^2)$	Δn_s	$\Delta\ln A_s$	$\Delta\tau$	$\Delta\bar{x}_{\rm H}(7.0)$[a]	$\Delta\bar{x}_{\rm H}(7.5)$	$\Delta\bar{x}_{\rm H}(8.0)$	$\Delta\Omega_{\rm k}$	Δm_ν (eV)	$\Delta\alpha$
LOFAR	OPT	0.025	0.27	0.44	0.063	0.89	...	...	...	...	0.14	0.87	0.027
	MID	0.13	0.083	0.15	0.36	0.80	...	...	...	...	0.35	12	0.17
MWA	OPT	0.046	0.11	0.19	0.022	0.37	...	...	...	...	0.056	0.38	0.013
	MID	0.22	0.017	0.029	0.097	0.76	...	...	...	...	0.13	9.6	0.074
SKA	OPT	0.0038	0.044	0.083	0.0079	0.16	...	...	...	...	0.023	0.12	0.0040
	MID	0.014	0.0049	0.0081	0.012	0.037	...	...	...	...	0.043	0.36	0.0060
FFTT	OPT	0.000 15	0.0032	0.0083	0.000 40	0.015	...	...	...	...	0.00098	0.011	0.000 34
	MID	0.000 41	0.000 38	0.000 62	0.000 36	0.0013	...	...	...	...	0.0037	0.0078	0.000 17
	PESS	1.1	0.017	0.037	0.010	0.19	...	...	...	...	...	0.20	0.0058
Planck		0.0070	0.0081	0.0059	0.0033	0.0088	0.0043	...	...	...	0.025	0.23	0.0026
+LOFAR	OPT	0.0066	0.0077	0.0058	0.0031	0.0088	0.0043	0.0077	0.0084	0.0093	0.0051	0.060	0.0022
	MID	0.0070	0.0081	0.0059	0.0032	0.0088	0.0043	0.18	0.26	0.23	0.018	0.22	0.0026
	PESS	0.0070	0.0081	0.0059	0.0033	0.0088	0.0043	0.54	0.31	0.24	0.025	0.23	0.0026
+MWA	OPT	0.0067	0.0079	0.0057	0.0031	0.0088	0.0043	0.0065	0.0067	0.0069	0.0079	0.027	0.0014
	MID	0.0061	0.0070	0.0056	0.0030	0.0087	0.0043	0.32	0.22	0.29	0.021	0.19	0.0026
	PESS	0.0070	0.0081	0.0059	0.0033	0.0088	0.0043	3.8	0.87	0.53	0.025	0.23	0.0026
+SKA	OPT	0.0031	0.0038	0.0046	0.0013	0.0087	0.0042	0.0060	0.0060	0.0060	0.0017	0.017	0.000 64
	MID	0.0036	0.0040	0.0044	0.0025	0.0087	0.0043	0.0094	0.014	0.011	0.0039	0.056	0.0022
	PESS	0.0070	0.0081	0.0059	0.0033	0.0088	0.0043	0.061	0.024	0.012	0.025	0.21	0.0026
+FFTT	OPT	0.000 15	0.0015	0.0036	0.000 21	0.0087	0.0042	0.0056	0.0056	0.0056	0.000 32	0.0031	0.000 094
	MID	0.000 38	0.000 34	0.000 59	0.000 33	0.0086	0.0042	0.0013	0.0022	0.0031	0.000 23	0.0066	0.000 17
	PESS	0.0055	0.0064	0.0051	0.0030	0.0087	0.0043	0.0024	0.0029	0.0040	0.025	0.020	0.0010

[a] $\bar{x}_{\rm H}(z)$ denotes the mean neutral fraction at the central redshift z. $\bar{x}_{\rm H}(z)$'s and A_s are completely degenerate from the 21 cm measurement alone. For this reason, the errors shown for $\ln A_{\rm s}$ from 21 cm data alone are really not marginalized over the $\bar{x}_{\rm H}(z)$'s.

gent constraints on $\Omega_{\rm k}$, m_ν, and α. For example, in the OPT model, from LOFAR/MWA/SKA/FFTT combined with Planck, the curvature density $\Omega_{\rm k}$ can be measured 5/3/15/78 times better, to a precision of $\Delta\Omega_{\rm k} = 0.005/0.008/0.002/0.0003$; the neutrino mass m_ν can be constrained 4/9/14/74 times better to an accuracy of $\Delta m_\nu = 0.06/0.03/0.02/0.003$; and running of the scalar spectral index α can be done 1/2/4/28 times better, to $\Delta\alpha = 0.002/0.001/0.0006/0.0001$. The more realistic MID model yields weaker yet still impressive constraints:

TABLE VI. The 1σ marginalized errors for the ionization parameters in the MID model. Assumptions are made the same as in Table V. $R_{\rm xx}$ and $R_{\rm x\delta}$ are in units of Mpc, and other parameters are unitless.

z		$\Delta b_{\rm xx}^2$	$\Delta R_{\rm xx}$	$\Delta\alpha_{\rm xx}$	$\Delta\gamma_{\rm xx}$	$\Delta b_{\rm x\delta}^2$	$\Delta R_{\rm x\delta}$	$\Delta\alpha_{\rm x\delta}$
7.0	Values	77	3.0	4.5	2.05	8.2	0.143	28
	LOFAR	94	140	130	27	5.1	49	9600
	MWA	20	43	43	8.3	2.6	16	3200
	SKA	9.1	9.8	8.7	2.0	0.49	2.6	520
	FFTT	0.59	0.47	0.39	0.098	0.027	0.088	17
7.5	Values	9.9	1.3	1.6	2.3	3.1	0.58	2
	LOFAR	2.2	55	18	73	1.4	5.7	24
	MWA	4.3	16	4.9	22	1.8	1.8	8.1
	SKA	0.18	1.7	0.71	2.1	0.076	0.17	0.78
	FFTT	0.0072	0.027	0.015	0.030	0.0023	0.0021	0.012
8.0	Values	2.12	1.63	−0.1	1.35	1.47	0.62	0.46
	LOFAR	1.6	20	2.1	34	1.2	3.4	6.9
	MWA	2.7	13	4.2	24	1.5	1.6	2.8
	SKA	0.085	0.60	0.090	0.90	0.057	0.095	0.24
	FFTT	0.0017	0.013	0.0026	0.017	0.0013	0.0014	0.0030

From SKA/FFTT combined with Planck, Ω_k can be measured 6/109 times better, to $\Delta\Omega_k = 0.004/0.0002$; m_ν 4/35 times better, to $\Delta m_\nu = 0.06/0.007$; and α 1/15 times better, to $\Delta\alpha = 0.002/0.0002$. The improved measurements of Ω_k and α enable further precision tests of inflation, since generically Ω_k is predicted to vanish down to the 10^{-5} level, while the simplest inflation models (with a single slow-rolling scalar field) predict $\alpha \sim (1 - n_s)^2 \sim 10^{-3}$. For example, the inflaton potential $V(\phi) \propto \phi^2$ predicts $\alpha \approx -0.0007$, while $V(\phi) \propto \phi^4$ predicts $\alpha = 0.008$. In addition, 21 cm data combined with CMB data from Planck can make accurate measurements in the mean neutral fraction $\bar{x}_H(z)$ at separate redshifts, outlining the full path of reionization, e.g. at the $\Delta\bar{x}_H(z) \sim 0.01/0.003$ level from SKA/FFTT data combined with Planck data.

2. OPT and MID models

For most 21 cm experiments, the OPT model yields stronger constraints than the MID model. The reason is as follows. By assuming $P_{xx} = P_{x\delta} = 0$, there are essentially no neutral fraction fluctuations in the OPT model. This means that this model is an ideal model in which the 21 cm power spectrum encodes cosmological information *per se*, since $P_{\Delta T}(\mathbf{k}) \propto \mathcal{P}_{\delta\delta}(k)$ at each pixel in the Fourier space. In the more realistic MID model, however, the nuisance ionization parameters have correlations with cosmological parameters. Mathematically, the inversion of a correlated matrix multiplies each error by a degradation factor.

An exception is the FFTT, where the situation is reversed. As mentioned in Sec. II B 2, the sample variance $P_{\Delta T}$ in the MID model is smaller than that in the OPT model for two reasons: (i) the MID model assumes nonzero P_{xx} and $P_{x\delta}$, and $P_{x\delta}$ has a negative contribution to the total power spectrum [see Eqs. (6) and (7)]; (ii) the OPT model assumes $\bar{x}_H = 1$, but $\bar{x}_H$ takes realistic values (less than 1) in the MID model, decreasing the overall amplitude. In a signal-dominated experiment, reduced sample variance can be more important than the degradation from correlations.

3. PESS model

Our results show that, even combined with CMB data from Planck, the 21 cm data using the PESS model cannot significantly improve constraints. There are two reasons for this failure. First, the PESS model essentially uses only $P_{\mu^4}(k)$ to constrain cosmology, by marginalizing over P_{μ^0} and P_{μ^2}. This loses a great deal of cosmological information in the contaminated P_{μ^0} and P_{μ^2}, in contrast to the situation in the OPT and MID models. Second, to effectively separate $P_{\mu^4}(k)$ from the other two moments, the available Fourier pixels should span a large range in μ. Figure 4 shows that in MWA and FFTT, the data set is a thin cylinder instead of a sphere. The limitation in the μ

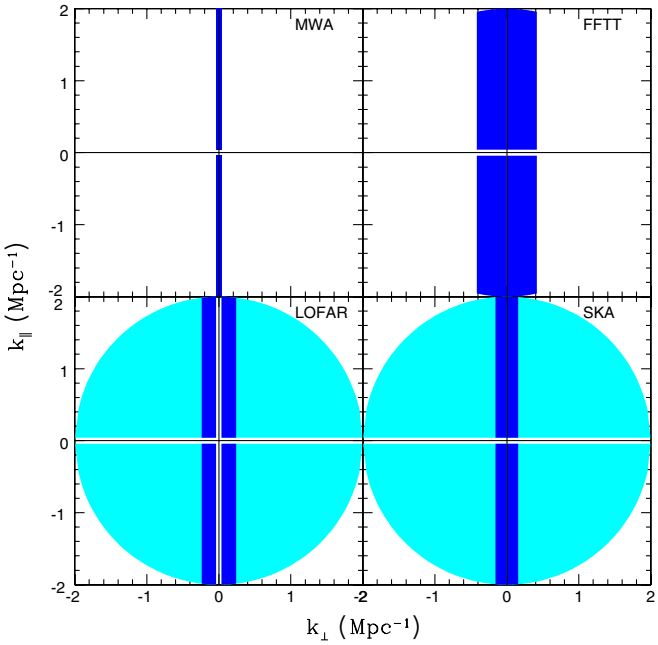

FIG. 4 (color online). Available $(k_\perp, k_\parallel)$ pixels from MWA (upper left), FFTT (upper right), LOFAR (lower left), and SKA (lower right), evaluated at $z = 8$. The blue/ gray regions can be measured with good signal-to-noise ratios from the nucleus and core of an array, while the cyan/light- gray regions are measured only with the annulus and have so poor signal-to-noise ratios that they hardly contribute to cosmological parameter constraints.

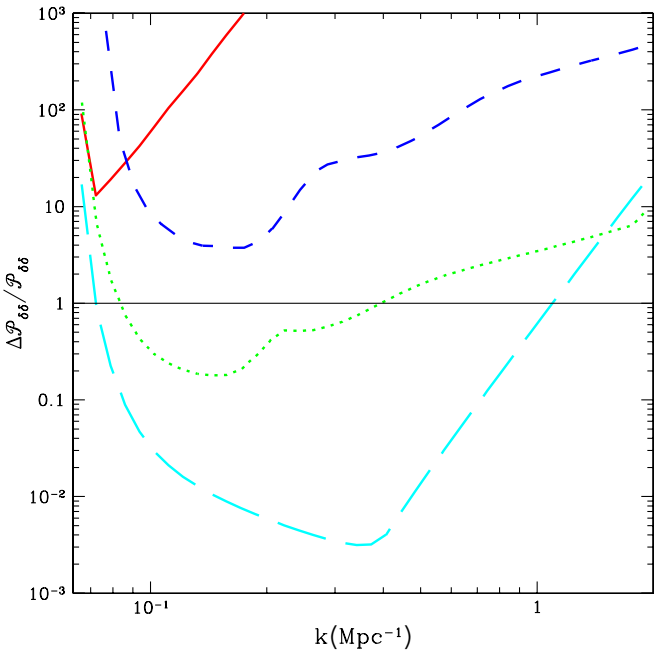

FIG. 5 (color online). Relative 1σ error for measuring $\mathcal{P}_{\delta\delta}(k)$ with the PESS model by observing a 6 MHz band that is centered at $z = 8$ with MWA (red/solid line), LOFAR (blue/short-dashed line), SKA (green/dotted line), and FFTT (cyan/long-dashed line). The step size is $\Delta \ln k \approx 0.10$.

range will give large degradation factors during the inversion of the Fisher matrix. (In the limit that there is only one μ for each shell, the Fisher matrix is singular and the degradation factor is infinite.) These two factors work together with the noise level to shrink the useful k modes into a rather narrow range: As shown in Fig. 5, $\Delta\mathcal{P}_{\delta\delta} < \mathcal{P}_{\delta\delta}$ only for $k = 0.09$–$0.4\ \mathrm{Mpc}^{-1}$ in SKA, $k = 0.07$–$1\ \mathrm{Mpc}^{-1}$ in FFTT and over zero modes in LOFAR and MWA.

B. Varying k_{max}

We test how varying k_{max} affects constraints in this section. The cutoff k_{max} depends on the scale at which nonlinear physics, e.g. the nonlinear clustering of density perturbations or the irregularities of ionized bubbles, enter the power spectrum. It is illustrated in the right panel of Fig. 6 that, generically, cosmological constraints asymptotically approach a value as k_{max} increases above $\sim 2\ \mathrm{Mpc}^{-1}$ (this typical scale can be larger for cosmic variance-limited experiments such as FFTT). Not much cosmological information is garnered from these high-k modes because detector noise becomes increasingly important with k. The upshot is that the accuracy only weakly depends on k_{max}.

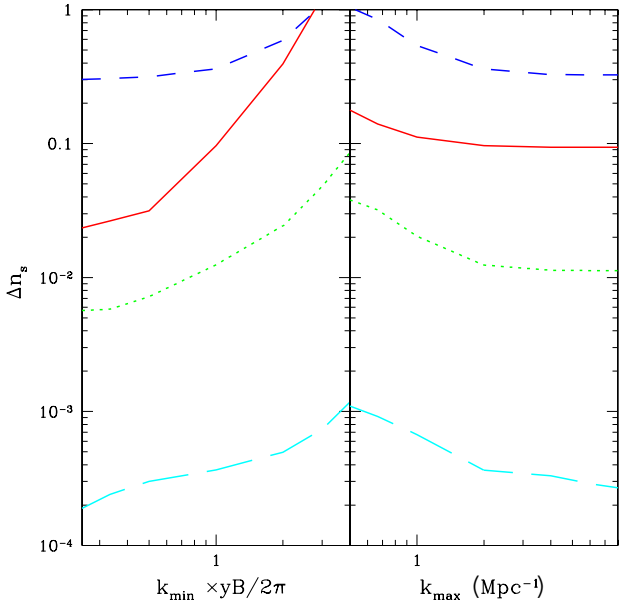

FIG. 6 (color online). How cosmological constraints Δn_s depend on k_{min} (left panel) and k_{max} (right panel) in the MID model with the 21 cm experiments MWA (red/solid line), LOFAR (blue/short-dashed line), SKA (green/dotted line), and FFTT (cyan/long-dashed line). We plot Δn_s in this example because it has the strongest dependence on k_{min} and k_{max} of all cosmological parameters. The quantity $2\pi/yB$ varies in redshift z bins, so as the horizontal axis of the left panel, we use the overall scale $\kappa_{\mathrm{min}} \equiv k_{\mathrm{min}} \times (yB/2\pi)$ which is equal for all z bins.

C. Varying the non-Gaussianity parameter ξ

Table II shows the effect of changing the non-Gaussianity parameter ξ in Sec. II D from the $\xi = 1$ (Gaussian) case to $\xi = 2$ in the PESS scenario, along with changing other assumptions. However, there is no need to perform an extensive numerical investigation of the impact of ξ, since it is readily estimated analytically. Because 1σ error Δp_i in cosmological parameters is $\sqrt{(F^{-1})_{ii}}$, it follows directly from Eq. (26) that Δp does not appreciably depend on ξ for noise-dominated experiments like MWA and LOFAR, whereas $\Delta p \propto \xi^{\sigma}$ with $\sigma \lesssim 1$ for (nearly) signal-dominated experiments like SKA and FFTT. Compared with the other effects that we discuss in this section, this (no more than linear) dependence on the non-Gaussianity parameter ξ is not among the most important factors.

D. Varying redshift ranges

We now test how accuracies depend on the redshift ranges. In Tables VII (OPT model) and VIII (MID model), we consider the optimistic/middle/pessimistic ranges, $z = 6.8$–$10/6.8$–$8.2/7.3$–8.2, which are divided by $n_z = 4/3/2$ z bins. The results show that, from 21 cm data alone, the constraints from the extreme ranges differ significantly (a factor of 5 for $\Delta\Omega_{\mathrm{k}}$). Therefore, the sensitivity of a 21 cm telescope depends strongly on the frequency range over which it can observe the signal.

E. Optimal configuration: Varying array layout

In this section we first investigate how the array layout affects the sensitivity to cosmological parameters. Next, we investigate the optimal array configuration for fixed number of antennae. Our parametrization of the array configuration is discussed in Sec. II G 2.

We map the constraint in m_ν on the $R_0 - R_{\mathrm{in}}$ plane in Fig. 7 (OPT model) and Fig. 8 (MID model). R_0 is the radius of the compact core, and R_{in} the radius of the inner core, both in units of $R_0^{\mathrm{max}} \equiv \sqrt{N_{\mathrm{in}}/\rho_0\pi}$. Note that if $R_0 = R_0^{\mathrm{max}}$, then $R_{\mathrm{in}} = R_0^{\mathrm{max}}$—this is the case of a "giant core," in which all antennae are compactly laid down with a physical covering fraction close to unity, and is represented by the x axis in the $R_0 - R_{\mathrm{in}}$ plane (the value of R_0 is meaningless if $R_{\mathrm{in}} = R_0^{\mathrm{max}}$). In Table IX, we list the optimal configuration that is indicated by Figs. 7 and 8. The compactness of an array is represented by $R_{\mathrm{in}}/R_0^{\mathrm{max}}$, since R_0^{max} is the minimum of R_{in}. In comparison, R_0/R_0^{max} does not indicate the compactness, since a slow falloff configuration with a small R_0 is effectively very close to a giant core. Rather, R_0 is a transition point from a flat, compact core to the falloff region. Note that we have three configuration parameters, R_0, R_{in}, and R_{out}. We find that the annulus for SKA and LOFAR makes almost no difference to the cosmological constraints, and therefore we focus on

TABLE VII. How cosmological constraints depend on the redshift range in the OPT model. Assumptions are the same as in Table V but for different redshift ranges, and we assume only the OPT model.

		Vanilla alone												
	z range	$\Delta\Omega_\Lambda$	$\Delta\ln(\Omega_m h^2)$	$\Delta\ln(\Omega_b h^2)$	Δn_s	$\Delta\ln A_s$	$\Delta\tau$	$\Delta\bar{x}_H(7.0)$	$\Delta\bar{x}_H(7.5)$	$\Delta\bar{x}_H(8.0)$	$\Delta\bar{x}_H(9.2)$	$\Delta\Omega_k$	Δm_ν (eV)	$\Delta\alpha$
LOFAR	6.8–10	0.021	0.20	0.34	0.049	0.67	...	...	...	...	...	0.086	0.75	0.023
	6.8–8.2	0.025	0.27	0.44	0.063	0.89	...	...	...	...	...	0.14	0.87	0.027
	7.3–8.2	0.036	0.38	0.61	0.090	1.2	...	...	...	...	...	0.24	1.3	0.038
MWA	6.8–10	0.037	0.072	0.14	0.016	0.25	...	...	...	...	...	0.031	0.31	0.011
	6.8–8.2	0.046	0.11	0.19	0.022	0.37	...	...	...	...	...	0.056	0.38	0.013
	7.3–8.2	0.070	0.15	0.27	0.032	0.51	...	...	...	...	...	0.097	0.53	0.018
SKA	6.8–10	0.0032	0.031	0.061	0.0058	0.12	...	...	...	...	...	0.012	0.096	0.0032
	6.8–8.2	0.0038	0.044	0.083	0.0079	0.16	...	...	...	...	...	0.023	0.12	0.0040
	7.3–8.2	0.0053	0.059	0.11	0.011	0.21	...	...	...	...	...	0.042	0.17	0.0054
FFTT	6.8–10	0.000 12	0.0023	0.0058	0.000 30	0.011	...	...	...	...	...	0.000 45	0.0073	0.000 23
	6.8–8.2	0.000 15	0.0032	0.0083	0.000 40	0.015	...	...	...	...	...	0.000 98	0.011	0.000 34
	7.3–8.2	0.000 21	0.0042	0.011	0.000 52	0.019	...	...	...	...	...	0.0021	0.014	0.000 43
Planck		0.0070	0.0081	0.0059	0.0033	0.0088	0.0043	...	...	...	...	0.025	0.23	0.0026
+LOFAR	6.8–10	0.0065	0.0076	0.0057	0.0031	0.0088	0.0043	0.0077	0.0084	0.0082	0.0090	0.0046	0.051	0.0021
	6.8–8.2	0.0066	0.0077	0.0058	0.0031	0.0088	0.0043	0.0077	0.0084	0.0093	...	0.0051	0.060	0.0022
	7.3–8.2	0.0068	0.0079	0.0058	0.0032	0.0088	0.0043	...	0.0085	0.0093	...	0.0072	0.081	0.0024
+MWA	6.8–10	0.0065	0.0076	0.0056	0.0031	0.0088	0.0043	0.0065	0.0067	0.0066	0.0067	0.0066	0.023	0.0013
	6.8–8.2	0.0067	0.0079	0.0057	0.0031	0.0088	0.0043	0.0065	0.0067	0.0069	...	0.0079	0.027	0.0014
	7.3–8.2	0.0068	0.0080	0.0058	0.0032	0.0088	0.0043	...	0.0067	0.0069	...	0.011	0.036	0.0017
+SKA	6.8–10	0.0027	0.0035	0.0045	0.0012	0.0087	0.0042	0.0060	0.0060	0.0060	0.0060	0.0016	0.015	0.000 61
	6.8–8.2	0.0031	0.0038	0.0046	0.0013	0.0087	0.0042	0.0060	0.0060	0.0060	...	0.0017	0.017	0.000 64
	7.3–8.2	0.0039	0.0047	0.0049	0.0017	0.0087	0.0042	...	0.0060	0.0060	...	0.0020	0.019	0.000 75
+FFTT	6.8–10	0.000 13	0.0014	0.0033	0.000 19	0.0087	0.0042	0.0054	0.0054	0.0054	0.0054	0.000 26	0.0025	0.000 078
	6.8–8.2	0.000 15	0.0015	0.0036	0.000 21	0.0087	0.0042	0.0056	0.0056	0.0056	...	0.000 32	0.0031	0.000 094
	7.3–8.2	0.000 20	0.0016	0.0038	0.000 23	0.0087	0.0042	...	0.0057	0.0057	...	0.000 40	0.0038	0.000 11

TABLE VIII. How cosmological constraints depend on the redshift range in the MID model. Assumptions are the same as in Table V but for different redshift ranges, and we assume only the MID model.

		Vanilla alone												
	z range	$\Delta\Omega_\Lambda$	$\Delta\ln(\Omega_m h^2)$	$\Delta\ln(\Omega_b h^2)$	Δn_s	$\Delta\ln A_s$	$\Delta\tau$	$\Delta\bar{x}_H(7.0)$	$\Delta\bar{x}_H(7.5)$	$\Delta\bar{x}_H(8.0)$	$\Delta\bar{x}_H(9.2)$	$\Delta\Omega_k$	Δm_ν (eV)	$\Delta\alpha$
LOFAR	6.8–10	0.090	0.055	0.093	0.18	0.43	...	...	...	...	...	0.22	5.7	0.080
	6.8–8.2	0.13	0.083	0.15	0.36	0.80	...	...	...	...	...	0.35	12	0.17
	7.3–8.2	0.21	0.099	0.15	0.42	0.81	...	...	...	...	...	0.62	15	0.18
MWA	6.8–10	0.15	0.012	0.020	0.031	0.46	...	...	...	...	...	0.092	4.4	0.025
	6.8–8.2	0.22	0.017	0.029	0.097	0.76	...	...	...	...	...	0.13	9.6	0.074
	7.3–8.2	0.40	0.018	0.030	0.099	1.0	...	...	...	...	...	0.32	18	0.083
SKA	6.8–10	0.010	0.0031	0.0056	0.0073	0.023	...	...	...	...	...	0.031	0.23	0.0032
	6.8–8.2	0.014	0.0049	0.0081	0.012	0.037	...	...	...	...	...	0.043	0.36	0.0060
	7.3–8.2	0.018	0.0050	0.0081	0.013	0.039	...	...	...	...	...	0.072	0.41	0.0063
FFTT	6.8–10	0.000 29	0.000 21	0.000 43	0.000 25	0.000 97	...	...	...	...	...	0.0020	0.0055	0.000 11
	6.8–8.2	0.000 41	0.000 38	0.000 62	0.000 36	0.0013	...	...	...	...	...	0.0037	0.0078	0.000 17
	7.3–8.2	0.000 50	0.000 39	0.000 62	0.000 37	0.0013	...	...	...	...	...	0.0058	0.0083	0.000 18
Planck		0.0070	0.0081	0.0059	0.0033	0.0088	0.0043	...	...	...	...	0.025	0.23	0.0026
+LOFAR	6.8–10	0.0069	0.0080	0.0058	0.0032	0.0088	0.0043	0.18	0.26	0.15	0.23	0.017	0.22	0.0026
	6.8–8.2	0.0070	0.0081	0.0059	0.0032	0.0088	0.0043	0.18	0.26	0.23	...	0.018	0.22	0.0026
	7.3–8.2	0.0070	0.0081	0.0059	0.0032	0.0088	0.0043	...	0.27	0.23	...	0.023	0.22	0.0026
+MWA	6.8–10	0.0056	0.0065	0.0054	0.0029	0.0087	0.0043	0.32	0.22	0.091	0.36	0.020	0.11	0.0025
	6.8–8.2	0.0061	0.0070	0.0056	0.0030	0.0087	0.0043	0.32	0.22	0.29	...	0.021	0.19	0.0026
	7.3–8.2	0.0061	0.0071	0.0056	0.0030	0.0087	0.0043	...	0.25	0.29	...	0.024	0.19	0.0026
+SKA	6.8–10	0.0025	0.0027	0.0038	0.0023	0.0087	0.0042	0.0094	0.014	0.0075	0.024	0.0032	0.033	0.0020
	6.8–8.2	0.0036	0.0040	0.0044	0.0025	0.0087	0.0043	0.0094	0.014	0.011	...	0.0039	0.056	0.0022
	7.3–8.2	0.0036	0.0041	0.0044	0.0025	0.0087	0.0043	...	0.015	0.011	...	0.0053	0.056	0.0023
+FFTT	6.8–10	0.000 33	0.000 21	0.000 43	0.000 24	0.0086	0.0042	0.0013	0.0022	0.0030	0.0040	0.000 20	0.0052	0.000 11
	6.8–8.2	0.000 38	0.000 34	0.000 59	0.000 33	0.0086	0.0042	0.0013	0.0022	0.0031	...	0.000 23	0.0066	0.000 17
	7.3–8.2	0.000 41	0.000 35	0.000 59	0.000 33	0.0086	0.0042	...	0.0022	0.0031	...	0.000 24	0.0070	0.000 17

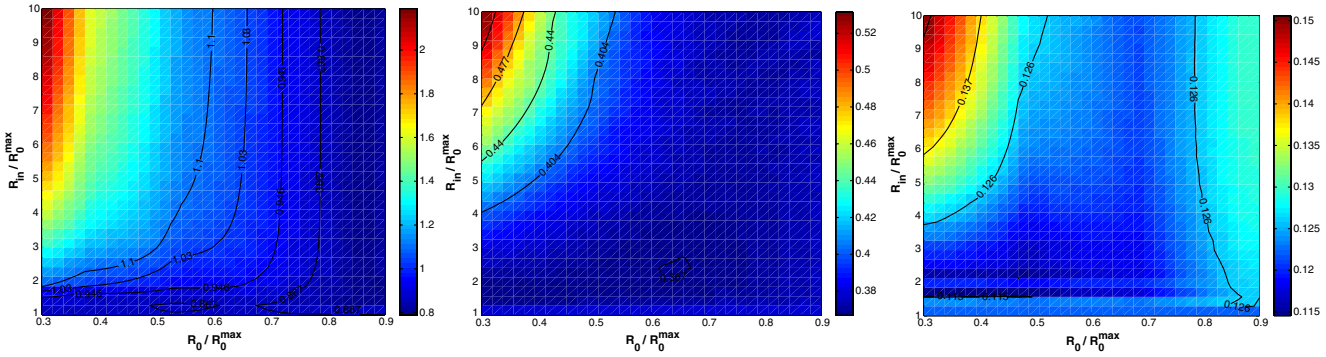

FIG. 7 (color online). The 1σ errors for m_ν marginalized over vanilla parameters for various configurations $(R_0, R_{\rm in})$ of LOFAR (left panel), MWA (middle panel), and SKA (right panel). We made the same assumptions here as in Table V but assume only the OPT model.

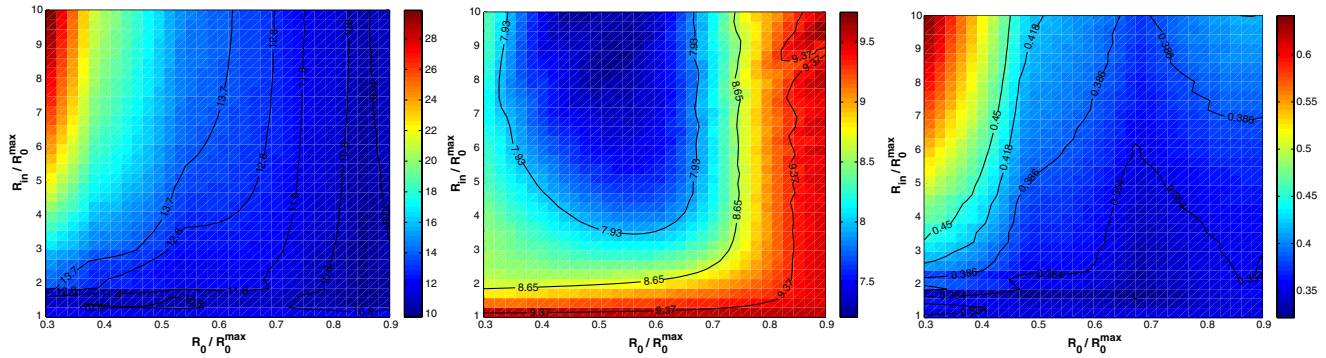

FIG. 8 (color online). Same as Fig. 7 but for the MID model. Figures are for LOFAR (left panel), MWA (middle panel), and SKA (right panel).

how to optimize only the remaining two parameters, R_0 and $R_{\rm in}$.

Table IX shows that the optimal layout for the OPT model is close to a giant core, with the inner core much smaller than previously proposed. For the MID model, LOFAR and SKA still favor the quasigiant-core layout, but MWA favors a large core whose radius is about the size that was previously proposed. The accuracies in m_ν vary in the OPT model by a factor of 3 for LOFAR and 1.4–1.5 for MWA and SKA, and in the MID model by a factor of 3 for LOFAR, 1.3 for MWA, and 2.2 for SKA. This means that an optimal configuration can improve the constraints by a factor up to 3 in noise-dominated experiments, and up to 2 in signal-dominated experiments.

The plots have three interesting features. First, the configuration of a quasigiant core is generically favored. The reason for this is that the noise on the temperature in an observing cell with $u_\perp$ is inversely proportional to the square root of the number of baselines that probe this $u_\perp$. A compact array increases the number of baselines that

TABLE IX. Optimal configuration for various 21 cm interferometer arrays. Assumptions are the same as in Table V but for a different array layout. $R_{\rm in}^{\rm prop}$ is the previously proposed inner core radius. η is the ratio of the number of antennae in the nucleus to the total number inside the core. n is the falloff index by which $\rho \propto r^{-n}$ outside the nucleus.

	Experiment	$R_0^{\rm max}$ (m)	$R_0(\times R_0^{\rm max})$	$R_{\rm in}(\times R_0^{\rm max})$	$R_{\rm in}^{\rm prop}$ (m)[a]	η	n	Comments
OPT	LOFAR	319	0.84	1.28	1000	0.71	6.0	Almost a giant core
	MWA	50	0.64	2.41	750	0.41	3.0	Close to a giant core
	SKA	211	0.30	1.56	1000	0.09	0.83	Almost a giant core
MID	LOFAR	319	0.84	1.28	1000	0.71	6.0	Almost a giant core
	MWA	50	0.45	10	750	0.20	2.3	Both a large nucleus and a widespread core
	SKA	211	0.68	1.57	1000	0.46	2.9	Almost a giant core

[a]Note that in LOFAR and SKA there is an annulus with the outer radius 6 km and 5 km, respectively. So for these $R_{\rm in}$ is not the size of the total array.

probe small $u_\perp$, reducing the overall noise level on these modes. Second, a couple of the upcoming 21 cm experiments favor the configuration that is close but not identical to a giant core. The reason for this is because arrays become sample variance limited once they have a certain number of baselines that probe a given $u_\perp$. A simple estimate on the signal-to-noise ratio for a compact MWA shows that on average $\mathcal{P}_{\delta\delta}/\bar{P}_N \approx 5$ at $k \sim 0.1$ Mpc^{-1} and $\mathcal{P}_{\delta\delta}/\bar{P}_N \approx 1/40$ at $k \sim 0.7$ Mpc^{-1}. Although moving more antennae to the center can increase the signal-to-noise ratio, the error cannot be reduced as much if modes are already dominated by the signal. Third, in the MID model, MWA favors a less compact core. This fact is due to the mixing between cosmological and ionization parameters. Remember that the off-diagonal elements in the Fisher matrix are proportional to the magnitude of ionization power spectra—the smaller the magnitude, the smaller the degradation factor and the more accurate the cosmological parameter measurement. Figure 2 illustrates that the ionization power spectrum generically falls off at large k such that a relatively large core, which is more sensitive to these large k, may actually improve parameter constraints. This factor appears to be important for MWA because, as Fig. 4 shows, a compactified MWA only occupies a rather narrow band in k space. This means that MWA has to expand significantly in order to use much larger k modes.

It came to our attention that Lidz *et al.* [45] performed an analysis of the optimal configuration for MWA. They concluded that the optimal layout for MWA is a giant core. This conclusion is slightly different than ours; we find that a compact but not exactly giant core is optimal for MWA. The work in [45] defines the optimal configuration to be the configuration that maximizes the total signal-to-noise ratio, while our definition is based on parameter constraints. In addition, the conclusion in [45] is based on the comparison of a giant core array configuration to one without a giant core, while we investigate a range of plausible configurations. It should be pointed out that both approaches should be tested with detailed simulations.

F. Varying the collecting area

The survey volume and the noise per pixel are both affected by changing the collecting area A_e because the solid angle a survey observes is $\Omega \approx \lambda^2/A_e$ and $P^N \propto 1/A_e^2$ [Eq. (33)]. For noise-dominated experiments, $\delta P_{\Delta T}/P_{\Delta T} \propto P^N/\sqrt{N_c} \propto A_e^{-2}/\sqrt{A_e^{-1}} = A_e^{-3/2}$, and for signal-dominated experiments, $\delta P_{\Delta T}/P_{\Delta T} \propto 1/\sqrt{N_c} \propto A_e^{1/2}$. If we parametrize the scaling of the error on a cosmological parameter as $\Delta p \propto (A_e)^\beta$, we have $-1.5 < \beta < 0.5$. A caveat is FFTT which has fixed $\Omega = 2\pi$, so $\delta P_{\Delta T}/P_{\Delta T} \propto A_e^0$ (signal dominated) or $\delta P_{\Delta T}/P_{\Delta T} \propto 1/A_e^2$ (noise dominated). Since FFTT is nearly signal dominated, $\beta \lesssim 0$.

We show how the collecting area affects the accuracy in Tables X (OPT model) and XI (MID model). In the OPT model, it appears that $\beta \approx -0.4$ for LOFAR, $|\beta| \lesssim 0.2$ for MWA, $|\beta| \lesssim 0.3$ for SKA, and $\beta \sim -0.1$ for FFTT. In the MID model, it appears that $\beta \sim -1.3$ for LOFAR, $\beta \sim -0.5$ for MWA, $\beta \sim -0.6$ for SKA, and $\beta \sim -0.3$ for FFTT. These exponents are compatible with the above arguments. The upshot is that varying A_e does not significantly affect parameter constraints.

TABLE X. How cosmological constraints depend on the collecting areas in the OPT model. Assumptions are the same as in Table V but for different collecting areas A_e, and we assume only the OPT model. The exponent β tells the rule of thumb of the A_e dependence of marginalized errors Δp, assuming $\Delta p \propto (A_e)^\beta$.

	A_e/A_e^{fid}[a]	$\Delta\Omega_\Lambda$	$\Delta \ln(\Omega_m h^2)$	$\Delta \ln(\Omega_b h^2)$	Δn_s	$\Delta \ln A_s$
LOFAR	2.0	0.020	0.24	0.40	0.048	0.80
	1	0.025	0.27	0.44	0.063	0.89
	0.5	0.039	0.40	0.62	0.10	1.3
	β	−0.48	−0.37	−0.32	−0.53	−0.35
MWA	2.0	0.057	0.11	0.22	0.021	0.41
	1	0.046	0.11	0.19	0.022	0.37
	0.5	0.042	0.11	0.19	0.027	0.37
	β	0.22	0	0.11	−0.18	0.07
SKA	2.0	0.0027	0.048	0.099	0.0077	0.19
	1	0.0038	0.044	0.083	0.0079	0.16
	0.5	0.0043	0.043	0.076	0.0089	0.15
	β	−0.34	0.08	0.19	−0.10	0.17
FFTT	2.0	0.000 14	0.0031	0.0082	0.000 37	0.015
	1	0.000 15	0.0032	0.0084	0.000 40	0.015
	0.5	0.000 17	0.0035	0.0086	0.000 46	0.016
	β	−0.14	−0.09	−0.03	−0.16	−0.05

[a] A_e^{fid} refers to the fiducial values assumed in Table IV and are not the same for different arrays.

TABLE XI. How cosmological constraints depend on the collecting areas in the MID model. Assumptions are the same as in Table V but for different collecting areas A_e, and we assume only the MID model. The exponent β tells the rule of thumb of the A_e dependence of marginalized errors Δp, assuming $\Delta p \propto (A_e)^{\beta}$.

	$A_e/A_e^{\rm fid}$	$\Delta\Omega_\Lambda$	$\Delta\ln(\Omega_m h^2)$	$\Delta\ln(\Omega_b h^2)$	$\Delta n_{\rm s}$	$\Delta\ln A_{\rm s}$
LOFAR	2.0	0.086	0.044	0.072	0.15	0.35
	1	0.13	0.083	0.15	0.36	0.80
	0.5	0.26	0.17	0.35	0.92	2.0
	β	−0.80	−0.98	−1.1	−1.3	−1.3
MWA	2.0	0.21	0.015	0.025	0.073	0.61
	1	0.22	0.017	0.029	0.097	0.76
	0.5	0.26	0.026	0.045	0.16	1.3
	β	−0.15	−0.40	−0.42	−0.57	−0.55
SKA	2.0	0.013	0.0049	0.0079	0.0092	0.032
	1	0.014	0.0049	0.0081	0.012	0.037
	0.5	0.016	0.0063	0.011	0.022	0.053
	β	−0.15	−0.18	−0.24	−0.63	−0.36
FFTT	2.0	0.000 36	0.000 37	0.000 61	0.000 32	0.0012
	1	0.000 41	0.000 38	0.000 62	0.000 36	0.0013
	0.5	0.000 52	0.000 41	0.000 66	0.000 46	0.0016
	β	−0.27	−0.07	−0.06	−0.26	−0.21

G. Varying observation time and system temperature

The detector noise is affected by changing the observation time and system temperature. From Eq. (33), the noise $P^N \propto T_{\rm sys}^2/t_0$. Therefore, for noise-dominated experiments, $\delta P_{\Delta T}/P_{\Delta T} \propto P^N/\sqrt{N_c} \propto T_{\rm sys}^2/t_0$, and for signal-dominated experiments, $\delta P_{\Delta T}/P_{\Delta T} \propto 1/\sqrt{N_c} \propto (T_{\rm sys}^2/t_0)^0$. Assuming that the errors in the cosmological parameter $\Delta p \propto (T_{\rm sys}^2/t_0)^{\epsilon}$, we have $0 < \epsilon < 1$.

Since $T_{\rm sys}^2$ and t_0^{-1} share the same exponent, we evaluate ϵ by varying only t_0 in Tables XII (OPT model) and XIII (MID model). It appears that on average $\epsilon \sim 0.5$ for LOFAR, $\epsilon \sim 0.3$ for MWA, $\epsilon \sim 0.3$ for SKA, and $\epsilon < 0.1$ for FFTT in the OPT model, and $\epsilon \sim 0.8$ for LOFAR, $\epsilon \sim 0.5$ for MWA, $\epsilon \sim 0.4$ for SKA, and $\epsilon \lesssim 0.1$ for FFTT in the MID model. These exponents are compatible with the expected $0 < \epsilon < 1$ from the above argument. The upshot is that the order unity changes in $T_{\rm sys}$ and t_0 play a marginal role in the accuracy for future signal-dominated experiments.

TABLE XII. How cosmological constraints depend on the observation time in the OPT model. Assumptions are the same as in Table V but for different observation time t_0, and we assume only the OPT model. The exponent ϵ tells the rule of thumb of the t_0 dependence of marginalized errors Δp, assuming $\Delta p \propto (t_0)^{-\epsilon}$. t_0 is in units of 4000 hours.

	t_0	$\Delta\Omega_\Lambda$	$\Delta\ln(\Omega_m h^2)$	$\Delta\ln(\Omega_b h^2)$	$\Delta n_{\rm s}$	$\Delta\ln A_{\rm s}$
LOFAR	4.0	0.014	0.17	0.28	0.034	0.56
	1	0.025	0.27	0.44	0.063	0.89
	0.25	0.055	0.56	0.88	0.14	1.8
	ϵ	0.49	0.43	0.41	0.51	0.42
MWA	4.0	0.040	0.081	0.16	0.015	0.29
	1	0.046	0.11	0.19	0.022	0.37
	0.25	0.059	0.15	0.27	0.038	0.52
	ϵ	0.14	0.22	0.19	0.34	0.21
SKA	4.0	0.0019	0.034	0.070	0.0054	0.13
	1	0.0038	0.044	0.083	0.0079	0.16
	0.25	0.0060	0.061	0.11	0.013	0.21
	ϵ	0.41	0.21	0.16	0.32	0.17
FFTT	4.0	0.000 14	0.0031	0.0082	0.000 37	0.015
	1	0.000 15	0.0032	0.0084	0.000 40	0.015
	0.25	0.000 17	0.0035	0.0086	0.000 46	0.016
	ϵ	0.07	0.04	0.02	0.08	0.02

TABLE XIII. How cosmological constraints depend on observation time in the MID model. Assumptions are the same as in Table V but for a different observation time t_0, and we assume only the MID model. The exponent ϵ tells the rule of thumb of the t_0 dependence of marginalized errors Δp, assuming $\Delta p \propto (t_0)^{-\epsilon}$. t_0 is in units of 4000 hours.

	t_0	$\Delta\Omega_\Lambda$	$\Delta \ln(\Omega_m h^2)$	$\Delta \ln(\Omega_b h^2)$	Δn_s	$\Delta \ln A_s$
LOFAR	4.0	0.061	0.031	0.051	0.11	0.25
	1	0.13	0.083	0.15	0.36	0.80
	0.25	0.36	0.24	0.50	1.3	2.9
	ϵ	0.64	0.74	0.82	0.89	0.88
MWA	4.0	0.15	0.010	0.017	0.052	0.43
	1	0.22	0.017	0.029	0.097	0.76
	0.25	0.36	0.037	0.064	0.23	1.8
	ϵ	0.32	0.47	0.48	0.54	0.52
SKA	4.0	0.0089	0.0035	0.0056	0.0065	0.022
	1	0.014	0.0049	0.0081	0.012	0.037
	0.25	0.023	0.0090	0.015	0.031	0.075
	ϵ	0.34	0.34	0.36	0.56	0.44
FFTT	4.0	0.000 36	0.000 37	0.000 61	0.000 32	0.0012
	1	0.000 41	0.000 38	0.000 62	0.000 36	0.0013
	0.25	0.000 52	0.000 41	0.000 66	0.000 46	0.0016
	ϵ	0.13	0.04	0.03	0.13	0.10

H. Varying the foreground cutoff scale $k_{\rm min}$

Finally, we test how accuracy is affected by varying $k_{\rm min}$above which foregrounds can be cleaned from the signal. One expects that the constraints tend to approach asymptotic values at small enough $k_{\rm min}$. However, the most effectively constrained modes are at small k ($k \sim 0.1\ {\rm Mpc}^{-1}$) for noise-dominated experiments, while the contributions from larger k modes are more important for cosmic variance-limited experiments. This means that $k_{\rm min}$ affects the noise-dominated experiments the most. The left panel of Fig. 6 illustrates this by plotting cosmological constraints as a function of the relative minimum cutoff $\kappa_{\rm min} \equiv k_{\rm min} \times y(z)B(z)/2\pi$, which is a constant scale factor for all z bins by definition. The slopes at $\kappa_{\rm min} = 1$ are rather large for MWA (varying from $\kappa_{\rm min} = 0.5$ to 2, the error in n_s varies from 0.032 to 0.39, about 10 times larger). For a signal-dominated experiment like SKA, the constraints can be off by a factor of 3, or for FFTT by a factor of 1.6. This suggests that, in general, $k_{\rm min}$ is among the top factors to affect cosmological constraints.

IV. CONCLUSION & OUTLOOK

A. Which assumptions matter most?

In Sec. III, we have quantified how cosmological parameter measurement accuracy depends on assumptions about ionization power modeling, reionization history, redshift range, experimental specifications such as the array configuration, and astrophysical foregrounds. We now return to the overarching question from Sec. I that motivated our study: Which of these assumptions make the most and least difference?

To quantify this, we consider two of the parameters for which 21 cm tomography has the most potential for improving on Planck CMB constraints based on our estimates: $\Omega_{\rm k}$ and m_ν. Figure 9 shows $\Delta\Omega_{\rm k}$ based on data from Planck plus SKA, as well as Δm_ν from Planck plus FFTT. Varying the ionization power modeling from PESS to OPT models improves the constraints on these two parameters by a factor of 6–15. From 21 cm data alone in the OPT model, the optimal array configuration can affect accuracies up to a factor 3 (Fig. 7), redshift ranges affect it by up to a factor of 5 (Table VII), and residual foregrounds affect it by up to a factor of 10 (Fig. 6, left panel). In summary, the assumptions can be crudely ordered by importance as ionization power modeling $\gg$ foregrounds $\sim$ redshift ranges $\sim$ array layout $> A_e \sim T_{\rm sys} \sim t_0 \sim k_{\rm max} \sim$ non-Gaussianity.

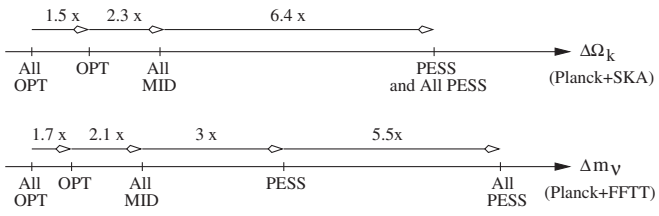

FIG. 9. Cartoon showing how cosmological parameter measurement accuracy depends on various assumptions. The cases labeled merely "PESS" or "OPT" have the PESS/OPT ionization power spectrum modeling with MID assumptions for everything else.

B. Outlook

We have investigated how the measurement of cosmological parameters from 21 cm tomography depends on various assumptions. We have found that the assumptions about how well the reionization process can be modeled are the most important, followed by the assumptions pertaining to array layout, IGM evolution, and foreground removal.

Our results motivate further theoretical and experimental work. On the theoretical side, it will be valuable to develop improved EoR data analysis techniques. The OPT approach is restricted to when neutral fraction fluctuations are not important, which is not an accurate approximation during the EoR. On the other hand, although the PESS approach is, in principle, insensitive to our poor understanding of reionization by marginalizing over it, in practice this approach destroys too large a fraction of the cosmological information to be useful. Hopefully more detailed EoR simulations will enable our MID approach to be further improved into a phenomenological parametrization of our ignorance that is robust enough to be reliable, yet minimizes the loss of cosmological information.[3]

On the experimental side, there are numerous complications that are beyond the scope of this paper, but that are important enough to deserve detailed investigation in future work. To what extent can radio-frequency interference be mitigated, and to what extent does it degrade cosmological parameter accuracy? This is particularly important for instruments in densely populated parts of the world, such as LOFAR. To what extent is the subtraction of the foreground point sources hampered by the complicated off-center frequency scaling of the synthesized beam? To what extent does the dramatic variation of the synchrotron brightness temperature across the sky affect our results and optimal array design? Performing a realistic end-to-end simulation of possible experiments (from sky signal to volts and back) should be able to settle all of these issues.

These are difficult questions, but worthwhile because the potential for probing fundamental physics with 21 cm tomography is impressive: A future square kilometer array optimized for 21 cm tomography could improve the sensitivity of the Planck CMB satellite to spatial curvature and neutrino masses by up to 2 orders of magnitude, to $\Delta\Omega_k \approx 0.0002$ and $\Delta m_\nu \approx 0.007$ eV, and detect at 4σ the running of the spectral index predicted by the simplest inflation models.

ACKNOWLEDGMENTS

The authors wish to thank Judd Bowman, Jacqueline Hewitt, and Miguel Morales for helpful discussions and comments. Y. M. thanks Yi Zheng for technical help. This work is supported by the U.S. Department of Energy (D.O.E.) under Cooperative Research Agreement No. DE-FC02-94ER40818, NASA Grant No. NAG5-11099 and No. NNG06GC55G, NSF Grant No. AST-0134999 and No. 0607597, and from the David and Lucile Packard Foundation and the Research Corporation. O. Z. was supported by the Berkeley Center for Cosmological Physics.

APPENDIX: χ^2 GOODNESS OF FIT IN THE MID MODEL

In this appendix, we elucidate some issues in separating cosmological information from astrophysics in the MID model, and give the χ^2 goodness-of-fit test.

The parametrization of ionization power spectra is based on the assumption that these power spectra are smooth functions of k, and therefore can be parametrized with as many parameters as necessary to fit the data at some accuracy. However, the separation of cosmology from astrophysics implicitly depends on another assumption that the shapes of ionization power spectra are distinguishable from that of the matter power spectrum, since one can only measure the *total* 21 cm power spectrum. Albeit sometimes the shape may be similar at small k (see the plateaus in the ratios of power spectra in Fig. 2), the slope and amplitude of ionization power spectra at the falloff region can, in principle, distinguish nuisance functions from the matter power spectrum, determine the overall amplitude, and in return use the data at small k to further constrain the nuisance parameters that correspond to the amplitudes.

An avalanche of data from upcoming 21 cm experiments can make it possible to justify the MID model with some parametrization of ionization power spectra. There are standard statistical methods for testing whether the parametrization is successful. We now give a compact description of the χ^2 goodness-of-fit test, and refer interested readers to [50] for a useful review on the statistics. Note that we did not implement the χ^2 test in this paper since this would need observational data. The description of the χ^2 test below is intended to complement the discussions of the MID model in the main part of this paper. We want to test the hypothesis H_0 that the parametrization with fitting parameter values is an accurate account of the ionization power spectra. The parameter vector to be fitted is $\Theta \equiv (\lambda_i (i = 1, \ldots, N_p), \beta_\alpha (\alpha = 1, \ldots, n_{\rm ion}))$, where N_p and $n_{\rm ion}$ are the number of cosmological and ionization parameters, respectively. The observed data vector is $\mathbf{y} \equiv (y_1, \ldots, y_N)$ where $y_i \equiv P_{\Delta T}(\mathbf{k}_i)$ at each pixel $\mathbf{k}_i$ labeled by $i = 1, \ldots, N$, where N is the total number of pixels. Assuming the Gaussian statistic in the measurements, the corresponding vector $\mathbf{F}$ for the expected value is $F(\mathbf{k}_i;\Theta) = (\mathcal{P}_{\delta\delta} - 2\mathcal{P}_{x\delta} + \mathcal{P}_{xx}) + 2(\mathcal{P}_{\delta\delta} - \mathcal{P}_{x\delta})\mu^2 + \mathcal{P}_{\delta\delta}\mu^4$, and the variance is $\sigma_i^2 \equiv (\delta P_{\Delta T}(\mathbf{k}_i))^2 = \frac{1}{N_c}[P_{\Delta T}(\mathbf{k}_i) + P_N(k_{i\perp})]^2$.

[3]It is also possible to constrain cosmological parameters using lensing of 21 cm fluctuations [46–49].

We can now compute χ^2:

$$\chi^2(\Theta) = (\mathbf{y} - \mathbf{F}(\Theta))^T C^{-1} (\mathbf{y} - \mathbf{F}(\Theta)), \quad \text{(A1)}$$

where C is the covariance matrix. If each measurement y_i is independent, then C becomes diagonal with $C_{ii} = \sigma_i^2$. Then Eq. (A1) is simplified to be

$$\chi^2(\Theta) = \sum_{i=1}^{N} \frac{[y_i - F(\mathbf{k}_i; \Theta)]^2}{\sigma_i^2}. \quad \text{(A2)}$$

We can define the p value as the probability, under the assumption of the hypothesis H_0, of obtaining data at least as incompatible with H_0 as the data actually observed. So

$$p = \int_{\chi^2(\Theta)}^{\infty} f(z; n_d) dz, \quad \text{(A3)}$$

where $f(z; n_d)$ is the χ^2 probability density function with n_d degrees of freedom $n_d = N - (N_p + n_{\rm ion})$. Values of the χ^2 probability density function can be obtained from the CERNLIB routine PROB [51]. To set the criterion, a fit is good if $p \geq 0.95$, i.e. the real data fit the parametrization better than the 95% confidence level.

[1] J. D. Bowman, M. F. Morales, and J. N. Hewitt, Astrophys. J. **661**, 1 (2007).
[2] M. McQuinn, O. Zahn, M. Zaldarriaga, L. Hernquist, and S. R. Furlanetto, Astrophys. J. **653**, 815 (2006).
[3] M. G. Santos and A. Cooray, Phys. Rev. D **74**, 083517 (2006).
[4] S. Wyithe, A. Loeb, and P. Geil, arXiv:0709.2955.
[5] http://www.lofar.org/.
[6] http://21cma.bao.ac.cn/, formerly known as the PaST (http://web.phys.cmu.edu/~past/).
[7] http://www.haystack.mit.edu/ast/arrays/mwa/.
[8] http://www.skatelescope.org/.
[9] P. Shapiro, K. Ahn, M. A. Alvarez, I. T. Iliev, H. Martel, and D. Ryu, Astrophys. J. **646**, 681 (2006).
[10] A. Lewis and A. Challinor, Phys. Rev. D **76**, 083005 (2007).
[11] G. B. Field, Proc. IRE **46**, 240 (1958).
[12] S. A. Wouthuysen, Astron. J. **57**, 31 (1952).
[13] J. R. Pritchard and S. R. Furlanetto, Mon. Not. R. Astron. Soc. **376**, 1680 (2007).
[14] S. R. Furlanetto, M. Zaldarriaga, and L. Hernquist, Astrophys. J. **613**, 1 (2004).
[15] M. G. Santos, A. Cooray, and L. Knox, Astrophys. J. **625**, 575 (2005).
[16] M. Zaldarriaga, S. R. Furlanetto, and L. Hernquist, Astrophys. J. **608**, 622 (2004).
[17] J. D. Bowman, M. F. Morales, and J. N. Hewitt, Astrophys. J. **638**, 20 (2006).
[18] M. Tegmark and M. Zaldarriaga, arXiv:0805.4414.
[19] S. R. Furlanetto, S. P. Oh, and F. Briggs, Phys. Rep. **433**, 181 (2006).
[20] G. B. Field, Astrophys. J. **129**, 525 (1959).
[21] R. Barkana and A. Loeb, Astrophys. J. **624**, L65 (2005).
[22] R. Barkana and A. Loeb, Astrophys. J. **626**, 1 (2005).
[23] E. W. Kolb and M. S. Turner, *The Early Universe* (Addison Wesley, New York, 1990).
[24] X. C. Mao and X. P. Wu, arXiv:0709.3871.
[25] T. C. Chang, U. L. Pen, J. B. Peterson, and P. McDonald, Phys. Rev. Lett. **100**, 091303 (2008).
[26] R. Barkana, Mon. Not. R. Astron. Soc. **372**, 259 (2006).
[27] A. Nusser, Mon. Not. R. Astron. Soc. **364**, 743 (2005).
[28] M. McQuinn, S. R. Furlanetto, L. Hernquist, O. Zahn, and M. Zaldarriaga, Astrophys. J. **630**, 643 (2005).
[29] O. Zahn, M. Zaldarriaga, L. Hernquist, and M. McQuinn, Astrophys. J. **630**, 657 (2005).
[30] M. McQuinn, L. Hernquist, M. Zaldarriaga, and S. Dutta, arXiv:0704.2239; M. McQuinn, A. Lidz, O. Zahn, S. Dutta, L. Hernquist, and M. Zaldarriaga, Mon. Not. R. Astron. Soc. **377**, 1043 (2007).
[31] O. Zahn, A. Lidz, M. McQuinn, S. Dutta, L. Hernquist, M. Zaldarriaga, and S. R. Furlanetto, Astrophys. J. **654**, 12 (2007).
[32] M. Tegmark, N. A. Taylor, and A. F. Heavens, Astrophys. J. **480**, 22 (1997).
[33] M. Tegmark, Phys. Rev. Lett. **79**, 3806 (1997).
[34] A. Lidz, O. Zahn, M. McQuinn, M. Zaldarriaga, and S. Dutta, Astrophys. J. **659**, 865 (2007).
[35] M. G. Santos, A. Amblard, J. Pritchard, H. Trac, R. Cen, and A. Cooray, arXiv:0708.2424.
[36] M. Tegmark, A. Vilenkin, and L. Pogosian, Phys. Rev. D **71**, 103523 (2005).
[37] M. Tegmark *et al.* (SDSS Collaboration), Phys. Rev. D **74**, 123507 (2006).
[38] R. T. Schilizzi, P. Alexander, J. M. Cordes, P. E. Dewdney, R. D. Ekers, A. J. Faulkner, B. M. Gaensler, P. J. Hall, J. L. Jonas, and K. I. Kellermann, SKA website, downloadable at http://www.skatelescope.org/PDF/Draft_specifications_10Sep07.pdf (2007).
[39] M. F. Morales and J. N. Hewitt, Astrophys. J. **615**, 7 (2004).
[40] M. F. Morales, Astrophys. J. **619**, 678 (2005).
[41] X. M. Wang, M. Tegmark, M. Santos, and L. Knox, Astrophys. J. **650**, 529 (2006).
[42] T. Di Matteo, B. Ciardi, and F. Miniati, Mon. Not. R. Astron. Soc. **355**, 1053 (2004).
[43] S. P. Oh and K. J. Mack, Mon. Not. R. Astron. Soc. **346**, 871 (2003).
[44] T. Di Matteo, R. Perna, T. Abel, and M. J. Rees, Astrophys. J. **564**, 576 (2002).
[45] A. Lidz, O. Zahn, M. McQuinn, M. Zaldarriaga, and L. Hernquist, arXiv:0711.4373.
[46] O. Zahn and M. Zaldarriaga, Astrophys. J. **653**, 922 (2006).
[47] R. B. Metcalf and S. D. M. White, Mon. Not. R. Astron.

Soc. **381**, 447 (2007).
[48] R. B. Metcalf and S. D. M. White, arXiv:0801.2571.
[49] P. Zhang, Z. Zheng, and R. Cen, Mon. Not. R. Astron. Soc. **382**, 1087 (2007).
[50] See e.g. Review of Statistics (Sec. 32) in W.-M. Yao *et al.*, J. Phys. G **33**, 1 (2006) and the 2008 edition available on the PDG web page (http://pdg.lbl.gov/).
[51] Available online at http://wwwasdoc.web.cern.ch/wwwasdoc/cernlib.html.